NASA CONTRACTOR REPORT

NASA CR-324

NASA CR-324

EXTREME VACUUM TECHNOLOGY DEVELOPMENTS

by Paul J. Bryant, Charles M. Gosselin,
and William W. Longley, Jr.

Prepared under Contract No. NASr-63(06) *by*
MIDWEST RESEARCH INSTITUTE
Kansas City, Mo.
for

NATIONAL AERONAUTICS AND SPACE ADMINISTRATION • WASHINGTON, D. C. • NOVEMBER 1965

EXTREME VACUUM TECHNOLOGY DEVELOPMENTS

By Paul J. Bryant, Charles M. Gosselin,
and William W. Longley, Jr.

Distribution of this report is provided in the interest of
information exchange.   Responsibility for the contents
resides in the author or organization that prepared it.

CONTENTS

SUMMARY

Several phases relating to the attainment, measurement and application of ultra-high vacuum environments are reported below. The phases covered are: development of a dual expansion nozzle for vapor-jet studies; determination of the gases present in UHV systems with oil diffusion and getter-ion pumping; measurements and theory on cryopanel operation; establishment of cold welding criteria; and determination of response characteristics for extreme high vacuum gauges and field emission microscopes.

A vapor nozzle with dual expansion chambers has been designed. Many people have dismissed the Florescu design on the basis of his ultimate pressure runs; however, those runs were vapor-pressure limited. The high velocity, low density upper jet does improve pump performance, but more definitive tests must be made.

An analysis of the gas species present in a UHV system with getter-ion and oil diffusion pumping has shown many interesting comparisons. An important discovery was made regarding the operation of traps above oil diffusion pumps. A combined cryogenic and chemical trap has shown the ability to give more reliable and economical service.

Experimental data for helium cryopumping at 4.28°K on a stainless steel cryopanel has been obtained. In addition, the physical adsorption isotherm based on a triangular site model has been improved in several ways. The energy contributions due to nearest neighbors have been evaluated on an improved model. The change in effective adsorption energy is notable. Predictions of the revised theory are presented.

A guidelines study on cold welding has been performed. The results from three cases may be summarized as follows. For the ideal case, when molecularly smooth cleaved crystals are permitted to reheal, cold welding takes place due to the large area of contact which is reformed at normal atomic lattice spacings. When structural metals with original or polished surfaces make touch contact after exposure to simulated space environments, cold welding does not take place. When structural materials are subjected to vibrational contact under a 250 psi normal load cold welding takes place to a greater extent in vacuum than at atmospheric pressure.

The response of magnetron gauges in their original form and with a cesiation treatment is reviewed. Numerous data have shown that a characteristic break from linearity and cutoff level exists for magnetron gauges and that the pressure values at which these characteristics occur can be lowered by a cesiation treatment. A field emission microscope has been constructed and tested.

I. INTRODUCTION

The simulation of a given vacuum or known environment is required by many research programs. The investigation of physical or chemical interactions between materials requires that the materials be pure, that the surface be clean, or that the test environment be known and controlled. The required level or accuracy for these conditions is often greater than present technology provides, especially in the case of space simulation.

For example, a number of space simulation experiments specify a vacuum of 10^{-13} torr. The attainment of this pressure level appears to be within the ability of present technology. However, the measurement of 10^{-13} torr is questionable. Only a few intricate research instruments for pressure estimation are capable of operating in this range, while standard techniques and commercial equipment give erroneous indications. Thus, the ability to measure a pressure of the level required for space simulation is, at best, uncertain. Present adsorption isotherm predictions for idealized conditions indicate, as mentioned above, that it should be possible to attain 10^{-13} torr or lower with liquid helium cryopumping techniques. However, the isotherms for vapor pressures versus quantities of various gas species cryosorbed by a given panel material are not complete. Thus, the length of time over which a specified pressure can be maintained is also uncertain.

We may summarize this general introduction to the problems of simulating the vacuum of space by observing that both the measurement and maintenance of such low pressures are beyond the normal range of standard technology. Some special techniques may be applied, but these research methods are still in the experimental stages. The development of several such areas of vacuum science and technology are described in this report.

II. DEVELOPMENT OF A DUAL EXPANSION NOZZLE FOR IMPROVED DIFFUSION PUMP OPERATION

A review of technical literature regarding diffusion pump operation has suggested that improvement of the vapor-jet pumping mechanism may be feasible. The problem, which has been identified,[1] is the maintenance of both high pumping speed and low back diffusion rates in the ultra-high vacuum range. Florescu[2,3] suggests that both a high velocity and a high concentration of working fluid are necessary to maintain good performance with a vapor jet. On this basis, Alexander's[4] results with jets of different density and

velocity are explained by noting that for high jet densities an appreciable rebounding of gas molecules was the limiting factor in pump speed, while for low jet densities there was an insufficient entrainment of gas molecules to maintain a high pumping speed.

Kennedy[5] has performed experiments which tend to support his hypothesis that random compression waves from eruptive boiling are an important source of backspreading, especially in baffled systems. Results obtained under this program have shown that pumping speed is lowered by overdriving the boiler temperature. The increase of fluid temperature does raise the jet velocity; however, the jet density rises even more rapidly. Partly due to the increase in concentration of vapor and partly due to the relatively low vapor velocity, increased backspreading of the vapor occurs at high-jet concentrations. The decrease of pumping speed on overdriving a pump is therefore believed to be due to this backspreading. The falloff in pump speed, as ultimate or desorption limited pressure is reached, does indicate a difference of various pump fluids in regard to behavior under overdriving. The competition between increased velocity and increased backspreading thus limits the useful heat input to a normal diffusion pump.

Data obtained with a single jet under various conditions[1] showed that the pumping speed reached a maximum and then began to fall off, as boiler pressure was raised. However, the pressure difference across the jet continued to increase with boiler pressure. These data may be interpreted as a confirmation of higher entrainment by a more dense jet; it also shows the deleterious effect upon entrainment caused by backspreading from a too dense jet. In addition, the experimental results indicated that the ability of a jet to withstand back diffusion is directly proportional to its density and that more of that ability could be realized if the competing process of backspreading could be reduced so that still higher boiler pressures could be employed.

The use of a dual expansion nozzle design was proposed by Florescu[2,3] as a means of reconciling the two competing factors described above. Such a jet consists of a main nozzle surrounded by an umbrella nozzle (see Fig. 1). The umbrella nozzle (according to Florescu's design) should have a greater expansion ratio than the main nozzle so that the umbrella jet will consist of a lower density stream than the main jet. The advantage of such a combination should be the reduction of backspreading, due to the lower density of the umbrella, and a large pressure difference across the main jet, due to its high density. The use of higher boiler pressures should then be possible since backspreading of the umbrella jet would be negligible until higher boiler pressures are applied.
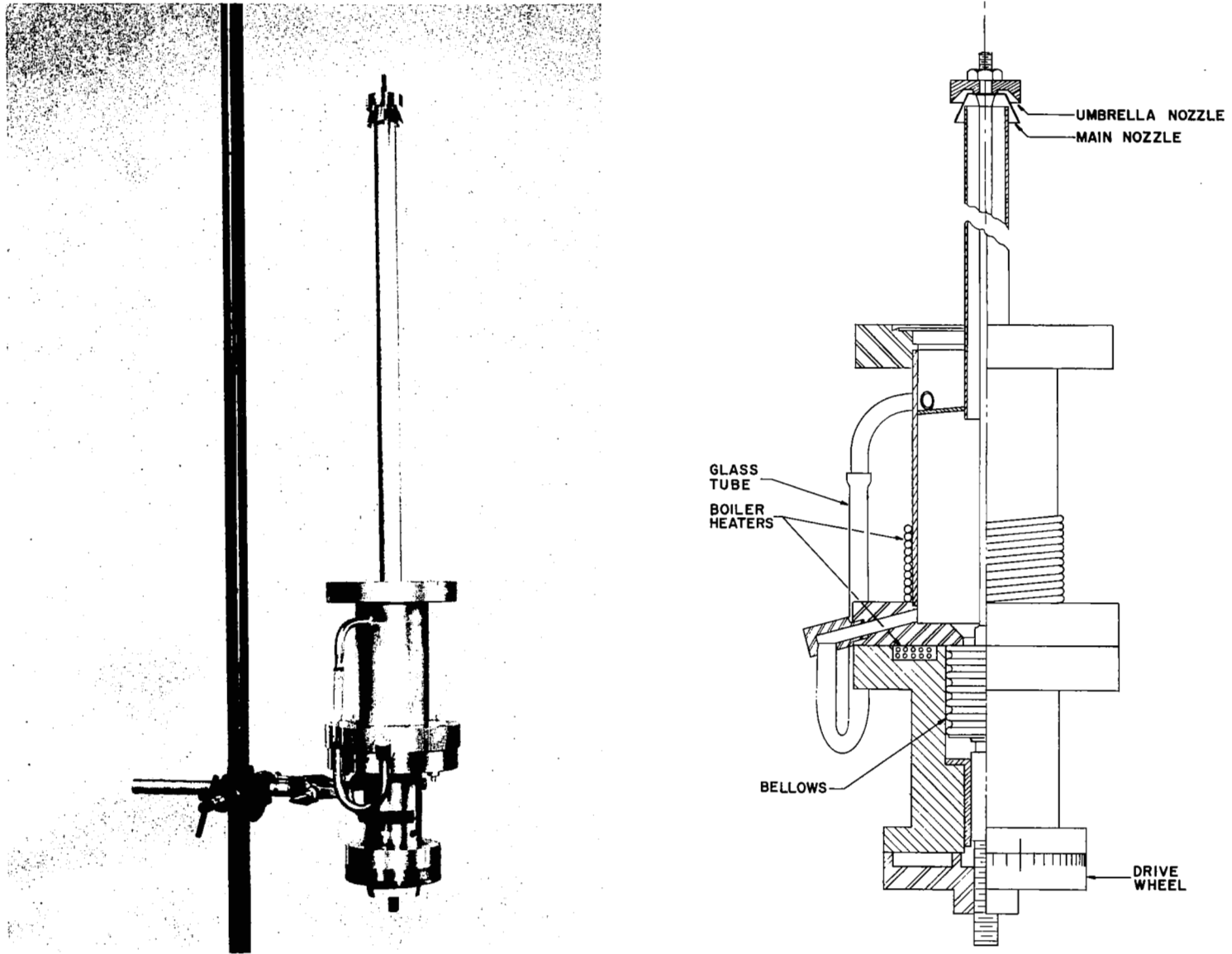
Fig. 1 - Diagram (Right) and Photograph (Left) of a Special Test Apparatus
for Evaluation of Experimental Diffusion Pump Nozzles. A Dual
Expansion Nozzle is Shown. The Drive Mechanism Provides for
Continuous Variation of Nozzle Gap During Operation.

A theoretical analysis conducted under this program found a possible mechanism for Florescu's indicated improvement and revealed a point that had been overlooked. Florescu[2] identified a reduced backspreading with the modified nozzle. This result may actually arise from the cross section for interaction between the umbrella jet and the backspreading molecules from the main jet. The interaction probability and the resulting momentum transfer from the high velocity umbrella molecules reduces backspreading from the main jet. Thus, the umbrella acts as a container for the main jet and reduces the deleterious effect upon pumping speed which is caused by backspreading molecules. In this manner the competing factors mentioned above may be reconciled. The increased velocity which results from the supersonic expansion in the umbrella nozzle probably accounts for the improved performance that Florescu observed. This increased velocity may also improve the entrainment of gas molecules by the vapor jet.

Florescu's experiments have been questioned because his ultimate pressure runs, which were made without degassing, showed no difference in ultimate pressure obtained. The Penning gauge or the lubricant used on the two-way stopcock may have caused this response, with the stopcock grease the more likely source of error. However, the metered leak runs at 2.5×10^{-5} torr intake pressure indicated that a modified jet has a 10 per cent improvement in pump speed at a given heater setting and a 22 per cent improvement in highest measured pump speed over a conventional nozzle design. The modified jet was the dual expansion nozzle with a strongly diverging umbrella nozzle and a cylindrical main nozzle. This improvement was attributed solely to the new design. The data do offer sufficient encouragement to justify an extension of the work into the ultra-high vacuum range.

A new system has been designed and constructed to test Florescu's predictions. Figure 1 shows both a cutaway drawing and a photograph of the new apparatus. A dual chamber nozzle is shown mounted on top of the boiler stack with a spoiler to divide the jet into two streams, one with high expansion ratio and, hence, high velocity and low density; and the other with moderate expansion ratio and, hence, lower jet velocity and higher density. The system is designed so that jet caps can be replaced when the pump is removed from the vapor-jet test apparatus.[1] The interchangeability of caps will permit tests with various cap designs.

The main feature of the assembly shown in Fig. 1 is a linear motion feedthrough by which the nozzle gap can be varied while the pump is operating. This feedthrough consists of the following units: a shaft to which the cap is attached; a section of thin wall stainless steel tubing in which thermocouples can be inserted to determine temperatures in the vapor column and the mercury

boiler; a bellows assembly at the bottom of the boiler to permit vertical displacement of the tube; a square shaft and square hole bushing to reduce the danger of twisting the bellows assembly; and a threaded shaft through a "micrometer" dial to indicate the nozzle gap. Both heater tapes and a ring heater are provided so that thermal gradients within the mercury can be controlled to reduce eruptive boiling. The nozzle gap can be varied to check the sensitivity of pump speed to nozzle spacing at a given boiler temperature. The present method of gap variation with a positive mechanical attachment will avoid the blow-off problem which was encountered at very high boiler pressures with the pump assembly described in Ref. 1.

Initial tests were run with the dual nozzle geometry shown in Fig. 1. The nozzle gap was varied over the full range of values to check the operation of the spoiler assembly. The densities of the umbrella jet and main jet were determined by means of the quantities of fluid transferred by each per unit time. Results consistently showed a higher transfer rate and thus a higher density for the main jet than for the umbrella jet. Thus, the larger expansion ratio of the umbrella nozzle together with the lower observed transfer rate assures a higher jet velocity as desired.

The results just listed demonstrate the basic operation of a dual expansion nozzle of the Florescu type. They also show the successful operation of our modified version of Florescu's design over the full range of gap variation provided. The vapor-jet test system has been redesigned to increase sensitivity so that data collected in the future may possibly show improved operation with a dual nozzle.

III. RESIDUAL GAS ANALYSIS OF UHV SYSTEMS

Analyses of the residual gases which are present in a well baked glass stainless steel vacuum system employing oil diffusion, ion, and getter-ion pumping are reported below.

The residual gases above an oil diffusion pump (using a special trap with and without chemicals) have been determined for various trapping conditions. The diffusion pump, special trap (which can be operated with or without chemicals)* and partial pressure analyzer (PPA) used in this work have been described earlier.[1] DC-705 silicone oil was chosen as the diffusion pump fluid. Preceding the gas analysis, the PPA system, the special trap, and the plumbing connecting the trap to the inlet of the diffusion pump were baked to 400°C. The total pressure in the system was from 2 to 4 x 10^{-9} torr. It has

---

* CVC Absorbant A.

been reported[1] that chemical traps operated at room temperature are not sufficient to reduce oil contamination in UHV systems which are evacuated by oil diffusion pump techniques. A study had been made of the effects of temperature on the ability of the trap operation with and without chemicals to reduce oil contamination.

The vacuum system used in this study was described previously.[1] However, two major modifications have been made as follows. (1) the getter-ion pump was isolated from the PPA system by a 1-1/2 in. valve. This change was necessary because the getter-ion pump had a measurable effect on the residual gases in a vacuum system (in the UHV range) even when it is not energized (e.g., desorption of gases such as argon and gettering of chemically active gases such as hydrogen); and (2) the 2.8 kilogauss permanent magnet originally used with the PPA was replaced with a 6.5 kilogauss electromagnet. The use of higher magnetic fields permitted greater resolution and sensitivity in the mass to charge ratio (m/e) range above 50. Also, linearity of response for the analyzer was improved by using magnetic scan techniques as compared to electrostatic scan techniques.*

The residual gases present in the UHV system when the special trap is operated with chemicals (CVC Absorbant type A) or without chemicals are listed in Table I. The trap temperatures employed for each case were established by liquid nitrogen or dry ice and acetone baths, or by ambient lab conditions. The background spectrum was determined while the PPA was isolated from all pumping units except a closed grid ion gauge.

The presence of helium in the background spectrum is due to permeation of helium through the glass envelope of the ion gauge. The partial pressure of helium is, therefore, a function of the length of time the UHV system is operated without the diffusion pump or getter-ion pump.

Hydrogen is always present, due to desorption from the metal parts in the UHV system. CO, CO_2, CH_4, and C_2H_6 are commonly found when hot tungsten filament devices are used (e.g., ion gauge or ion source for PPA).

---

* The number of ions which are drawn out of the ion cage of the PPA is dependent on the potential applied to the drawout electrodes. This voltage should be constant throughout an operational cycle. However, varying the accelerating potential during a scan (as is done in an electrostatic scanning device) has an effect on the drawout potential field. Thus, the resulting change in the number of ions drawn out of the ion cage is partially responsible for nonlinear response of the PPA.

RESIDUAL GASES IN AN OIL DIFFUSION PUMPED UHV SYSTEM FOR SEVERAL TRAPPING CONDITIONS

GAS	BACK GROUND	CHEMICAL IN TRAP			NO CHEMICAL IN TRAP		
		$-196°C$	$-78°C$	$25°C$	$-196°C$	$-78°C$	$25°C$
H_2	1.3×10^{-10}	2.1×10^{-9}	2.1×10^{-9}	1.8×10^{-9}	3.1×10^{-9}	2.5×10^{-9}	2.2×10^{-9}
He	5.1×10^{-11}	—	—	—	—	—	—
CH_4	2.2×10^{-10}	1.7×10^{-11}	6.8×10^{-11}	7.1×10^{-11}	1.6×10^{-11}	8.3×10^{-11}	1.3×10^{-10}
H_2O	1.6×10^{-12}	8.4×10^{-12}	8.7×10^{-12}	7.3×10^{-12}	9.4×10^{-12}	5.0×10^{-12}	6.3×10^{-12}
C_2H_2	—	—	—	—	—	—	1.3×10^{-12}
C_2H_4	—	1.1×10^{-12}	4.8×10^{-12}	3.3×10^{-11}	6.1×10^{-12}	8.8×10^{-11}	1.2×10^{-10}
CO	7.8×10^{-11}	1.5×10^{-11}	2.1×10^{-11}	5.7×10^{-11}	2.1×10^{-11}	1.3×10^{-10}	2.0×10^{-10}
C_2H_6	3.4×10^{-12}	1.3×10^{-12}	8.2×10^{-12}	9.5×10^{-12}	1.2×10^{-12}	7.8×10^{-12}	1.9×10^{-11}
A	5.8×10^{-13}	—	—	—	—	—	—
C_3H_6	—	6.3×10^{-13}	7.2×10^{-13}	2.1×10^{-12}	4.7×10^{-13}	2.2×10^{-12}	4.6×10^{-12}
CO_2	2.6×10^{-12}	2.1×10^{-12}	2.4×10^{-12}	3.6×10^{-12}	2.6×10^{-12}	3.8×10^{-12}	4.5×10^{-12}
C_4H_8	—	—	—	—	3.6×10^{-13}	8.3×10^{-13}	2.3×10^{-12}
C_6H_6	—	8.4×10^{-14}	1.8×10^{-12}	1.1×10^{-10}	6.4×10^{-13}	6.3×10^{-10}	5.3×10^{-10}
C_7H_8	—	—	—	—	—	—	2.3×10^{-12}
C_8H_{10}	—	—	—	—	—	3.0×10^{-13}	9.1×10^{-13}
TOTAL	4.8×10^{-10}	2.1×10^{-9}	2.2×10^{-9}	2.1×10^{-9}	3.2×10^{-9}	3.8×10^{-9}	3.3×10^{-9}

TABLE I - All significant gas species which constitute the total pressure are listed for each case. DC-705 oil was used; benzene (C_6H_6) is a characteristic gas. Note the values (torr, air equivalent) of benzene for each condition.

The sensitivity of the PPA for a given gas is not only dependent upon the operating electrical conditions (i.e., ionization potential and current, drawout potential, acceleration potential, focusing potentials and ion collector potentials),but also upon the work function of the dynode surfaces in the ion detector. The work function of these surfaces can vary due to the effects of a bakeout, cesiation,[1]/ or contamination such as the build-up of adsorbed layers of hydrocarbons. Because of the changing character of the ion detector, the PPA was used to obtain relative intensities for the various gases. Partial pressure values (in equivalent air units) were obtained for the various gas species by combining the PPA data with the reading of a closed grid ion gauge by means of the following calculations.

Consider the expression:

$$P = \sum_i p_i \quad ,$$

where

P = total pressure, and

p_i = partial pressure of the ith gas.

For an ionization gauge:

$$p_i = S_i I_i \quad ,$$

where

S_i = sensitivity of the ionization gauge for the ith gas, and

I_i = ion current due to the ith gas generated in the ionization gauge.

Further,

$$S_i = F_i S \quad ,$$

where F_i = gauge constant for the ith gas, and

              S = sensitivity for a gas chosen to be the standard, e.g.,dry air.

Also,

$$I_i = a_i I \quad ,$$

where a_i = per cent of total ion current due to the ith gas, and

            I = total ion current.

Therefore,

$$P = SI \sum_i a_i F_i \quad ,$$

but

$$SI = P' \quad ,$$

where P' = indicated total pressure (air equivalent units)

so that

$$P = P' \sum_i a_i F_i \quad ,$$

which implies that

$$P_i = P' a_i F_i \quad .$$

Expressed in equivalent air units,

$$p_i' = P' a_i = p_i \text{ (equivalent air units)} \quad .$$

Now for the PPA

$$p_i = \sum_j \bar{F}_i b_{ij} \bar{S} I_{ij}$$

where $\quad \bar{F}_i$ = gauge constant for i^{th} gas,

b_{ij} = collector efficiency of the ion detector for the jth cracking product of the ith gas,

$\bar{S}$ = sensitivity of the PPA for dry air, and

I_{ij} = ion current due to the jth cracking product of the ith gas.

For these calculations, it will be assumed that:

$$b_{ij} = 1$$

$$\sum_j I_{ij} \alpha I_i \text{ , and}$$

$$F_i = \bar{F}_i \quad .$$

These assumptions imply that

$$a_i = \frac{I_i}{\sum_i I_i} = \frac{\sum_j I_{ij}}{\sum_{ij} I_{ij}}$$

Therefore, a_i can be determined by means of the PPA and applied to the equation

$$p_i' = P' a_i \quad \text{in air equivalent units.}$$

11

To convert these values to true partial pressure values, the set of gauge constants (F_i) is needed,* i.e.,

$$p_i' = P'a_i F_i \quad .$$

Surface generated ions[1] are not listed in the table, since they do not have an observable effect on the residual gas. However, surface ions of Li, O, F, Na, and Cl were detected during this study.

Reviewing the data presented in Table I, it is noted that benzene is the best indicator of the presence of diffusion pump products in the system. At LN_2 temperature, both trapping conditions (i.e., with or without chemicals) are favorable for UHV operation. However, at dry ice acetone temperature, a difference of two and one-half orders of magnitude is noted. In this temperature range, the presence of chemicals demonstrates a significant advantage. The data also suggest that a chemical trap cooled to -78°C by mechanical refrigeration would provide effective trapping (even compared to a nonchemical trap at -196°C). The maintenance of liquid nitrogen traps has long been a problem. Fluctuation of the nitrogen level or loss of the coolant during a long term experiment has often nullified the experimental results. The results obtained in this study show that the use of mechanically refrigerated chemical traps should prove to be very useful for vacuum systems employing oil diffusion pumps.

The residual gases present in the above described UHV system, when evacuated by a getter-ion pump only, have also been determined. The data which were taken following a 400°C bake are presented in Table II. Again, pressures are given in equivalent air units.

To obtain true partial pressure values each of the measurements given in Table II must be corrected by the gauge factors, F_i . The primary gases, hydrogen and carbon monoxide, are typically found in metal systems in which hot tungsten filaments are used.

---

* Published gauge factors for Varian closed grid ion gauge are H_2 - 1.8, N_2 - 0.9, O_2 - 1.1, He - 5.6, H_2O - 1.0, CO_2 - 0.66, CO - 0.85, Hg - 0.26, A - 0.76, Ne - 3.8, Kr - 0.48, Xe - 0.33, air - 1.0

TABLE II

RESIDUAL GASES IN A STAINLESS STEEL SYSTEM AT ULTIMATE
PRESSURES WITH GETTER-ION PUMPING

H_2	1.1×10^{-10}
CO	1.8×10^{-10}
CH_4	1.6×10^{-11}
H_2O	3.3×10^{-12}
A	1.6×10^{-12}
CO_2	5.5×10^{-12}
C_2H_6	4.9×10^{-13}
C_2H_4	5.2×10^{-12}
Total	3.2×10^{-10} torr

IV. A STUDY OF CRYOPUMPING FOR INERT GASES

Two specific approaches have been applied to the investigation of cryopanel action for helium gas. A theoretical model has been refined and employed to compute helium adsorption isotherms. Experimental data were obtained for helium adsorption on a stainless steel cryopanel. Both the theoretical and experimental approaches are treated in detail in the following subsections.

A. Physical Adsorption Isotherm Theory

The physical adsorption isotherm theory developed earlier[1] has been revised by improving the energy expressions for the monolayers adsorbed. The triangular site model, shown in Fig. 2, is used in preference to the BET linear model. The effect of the introduction of an energy which is dependent on adsorbed particle interactions and an improved treatment of nearest neighbor interactions on the mathematical expressions is indicated.

When the dependence of the energy of a particle in one layer of adsorbed gas on the presence of all other layers is included in the energy constraint equation (Section III.A of Ref. 1), the relation becomes

$$dE = \sum_{j=1}^{\infty} \epsilon_{gj} \, dn_{gj} - \sum_{j=1}^{M} E_j \, dX_j = 0 \quad , \qquad (1)$$

TOP
VIEW

SIDE
VIEW

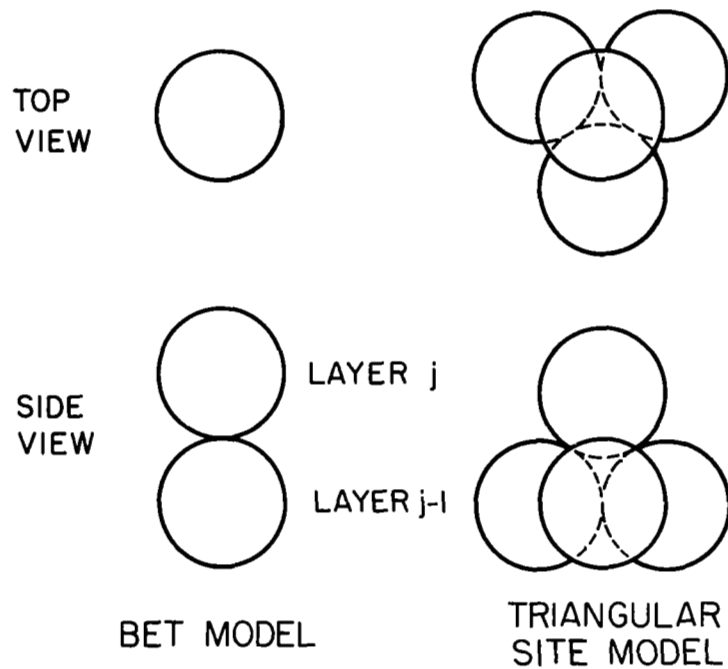LAYER j

LAYER j-I

BET MODEL

TRIANGULAR
SITE MODEL

Fig. 2 - Site Models, Showing the Geometric
Arrangement of Atomic Adsorption
Which is Assumed for the Develop-
ment of the BET Theory (Left) and
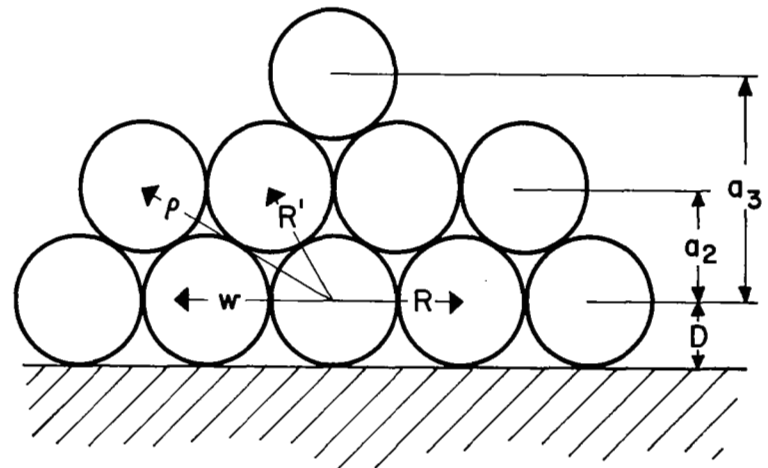for the Present Theory Based on a
Triangular Array (Right).

Fig. 3 - The Geometry of Adjacent Sites is
Shown According to the Triangular
Site Model. Nearest Neighbor,
Next Nearest Neighbor, and Inter-
layer Distances are Shown. The
First layer is Located a Distance
D Above the Effective Center of
the First Layer of Adsorbent
Molecules.

where ϵ_{gj} is the energy of the jth energy level in the gas, n_{gj} is the number of gas particles occupying this level, E is the total energy of the system, X_j is the number of particles in the jth adsorbed layer, there are M adsorbed layers which have nonzero occupation numbers, and E_j is the effective adsorption energy. The effective adsorption energy is defined in terms of the energy of adsorption for a particle in the jth layer, W_j , and the coverage of the jth layer, θ_j , by the expression

$$E_j = W_j + \sum_{i=1}^{M} \theta_i \frac{dW_i}{d\theta_j} \quad . \tag{2}$$

The expression for γ_j from Eq. (21) Ref. 1, must be set equal to the expression

$$\gamma_j = \frac{Km^{3/2}T^{5/2}}{p} e^{-E_j/k_o t} \quad , \tag{3}$$

where p is the pressure, m is the mass of a gas particle, T is the absolute temperature, k_o is the Boltzmann constant, and K is a function of physical constants explicitly indicated in Eq. (52) of Ref. 1.

The energy of adsorption for a particle in the jth layer is still treated as a sum of an adsorbate energy and the interaction energy with all other adsorbed particles. Although the numerical calculations are based on a Lennard-Jones (6-12) potential, the expressions for the energy are no longer based on an (n-2n) potential, but on a general potential with an attractive $-n^{th}$ power portion and a repulsive $-m^{th}$ power portion. We still retain the requirement that the attractive potential power be greater than three. The following expressions give the adsorbent contribution to the energy of adsorption:

$$W_s = 2\pi\epsilon_I N_o D^3 \left(\frac{k}{\ell-2} \right)^{\frac{k}{k-\ell}} \left(\frac{k-2}{\ell} \right)^{\frac{\ell}{k-\ell}} \frac{1}{(k-3)(\ell-3)} \quad , \tag{4}$$

15

$$W_{sj} = \frac{W_s}{k-\ell} \left[\frac{k-3}{(1+a_j/D)^{\ell-3}} - \frac{\ell-3}{(1+a_j/D)^{k-3}} \right] \quad , \tag{5}$$

where ϵ_I is the maximum attractive energy in the $(\ell-k)$ curve for the interaction between one gas particle and one atom from the adsorbate, D is the equilibrium distance between the centers of the particles adsorbed in the first layer and a representative surface, N_O is the density of adsorbate molecules, and a_j is the distance between the plane of centers for layer j and the plane of centers for layer one. Figure 3 shows D and a_j as well as the dimensions used in the calculation of cooperative interaction of the adsorbed particles.

For adsorbed particles which are not nearest neighbors, the z-function developed earlier is still used, but it is generalized to an (n-m) potential,

$$z(r) = \frac{\pi \epsilon \sigma_O r^2}{m-n} \left(\frac{m^m}{n^n} \right)^{\frac{1}{m-n}} \left[\frac{1}{n-2} \left(\frac{\sigma}{r} \right)^n - \frac{1}{m-2} \left(\frac{\sigma}{r} \right)^m \right] \tag{6}$$

where ϵ is the maximum attractive energy between two particles, σ is the distance of closest approach, and σ_O is the number of adsorbed molecules per unit area in a complete layer. If the ith layer has no sites with a nearest neighbor relation to the particle of the jth layer under consideration, it contributes an amount to W_j of W_{ij}, where

$$W_{ij} = \theta_i z(|a_i - a_j|) \quad . \tag{7}$$

Except for layer $j=1$, there is one layer in which three nearest neighbors are guaranteed, the $j-1$ layer, with a contribution

$$W_{j-1,j} = \theta_{j-1} z(\rho) - \frac{3}{2} \varphi(R') \quad , \tag{8}$$

16

where R' is the nearest neighbor distance for two layers and ρ is chosen to make $z(\rho)$ equal to the contribution from the next nearest neighbors in layer $j-1$. Now one has to consider the probability of nearest neighbors in the j and $j+1$ layers. A decent approximation to this probability can be obtained with the function P_j defined as follows:

$$P_j = \frac{\theta_{j+1}}{3\theta_j^3} P_{j-1}^2 \quad , \quad P_o = 3\theta_1 \tag{9}$$

By using this function, one can write the last two contributions to the cooperative energy as follows:

$$W_{j+1,j} = \theta_{j+1} z(\rho) - \frac{P_j}{2} \varphi(R') \quad , \tag{10}$$

$$W_{jj} = \theta_j z(w) + P_{j-1} \epsilon \quad , \tag{11}$$

where w is chosen to make $z(w)$ equal to the contribution from all second-nearest neighbor sites in the same layer.

The energy of adsorption can now be written

$$W_j = W_{sj} - \frac{1}{2}(3f_j' + P_j)\varphi(R') + P_{j-1}\epsilon + \theta_j z(w) + (f_j'\theta_{j-1} + \theta_{j+1})z(\rho)$$

$$+ \sum_{i=1}^{j-2} \theta_i z(a_j - a_i) + \sum_{i=j+2}^{M} \theta_i z(a_i - a_j) \tag{12}$$

where f_j' is one when j is not one and zero when j is one. The effective adsorption energy can be developed from Eqs. (2) and (12) and written as:

$$E_j = W_{sj} + 2P_{j-1}\epsilon - \frac{1}{2}(3+P_{j-1}\theta_{j-1}/\theta_j)f_j'\varphi(R') - \sum_{i=j+1}^{M} 2^{i-j-1}\theta_i$$

$$\times\left[P_{i-1}\epsilon - P_i\varphi(R')\right]/\theta_j + 2\theta_j z(w) + 2(f_j'\theta_{j-1}+\theta_{j+1})z(\rho)$$

$$+ 2\sum_{i=1}^{j-2}\theta_i z(a_j-a_i) + 2\sum_{i=j+2}^{M}\theta_i z(a_i-a_j) \quad . \tag{13}$$

The effect of varying the energy treatment from that used in Ref. 1 is seen by comparing Fig. 4a for helium on glass at 4.28°K with Figs. 19 and 20 of Ref. 1. A demonstration that the energy dependence does not always lead to a stepwise isotherm is possible as shown by Fig. 4b for helium on glass at 77°K. For simplicity, an ideal hexagonal close-packed structure has been assumed for multilayer configurations, thus $\varphi(R')$ has been set equal to $-\epsilon$.

The low temperature case, shown in Fig. 4a, consists of sharp step-wise coverage of the surface with monolayers of helium. The approximate theory curve neglects the interaction between helium particles in the same layer, thus not showing the steep rise of the exact theory. The logarithmic pressure scale is a convenient way to show the fast completion of the steps. The rise of the energy of adsorption, W_j , with pressure is shown. The lower portion of Fig. 4a shows the variation of effective adsorption energy, E_j , with pressure and demonstrates a rapid decrease in the effective energy in low layers as higher layers are filled. One can speculate that when the effective energy of a higher site is higher than the effective energy of a lower site, there could be a redistribution of particles from the lower layer to available sites in the higher layer until either all permitted sites in the higher layer are filled or the effective adsorption energies are equalized. Such a transition from two dimensional to three dimensional condensation could suggest drop-let formation on a uniform surface; however, the few numerical examples per-formed have had both layers essentially complete or a severe restriction on number of available sites in the higher layer, thus ruling out migration from layer to layer.

The isotherm for helium on glass at 77°K is plotted in Fig. 4b. A linear plot of pressure is used to show the smoothness of the isotherm. The partial occupancy of the individual layers is also shown. The energies of adsorption are monotonically increasing functions of pressure. The effective adsorption energy, including interlayer interaction energy effects, is also
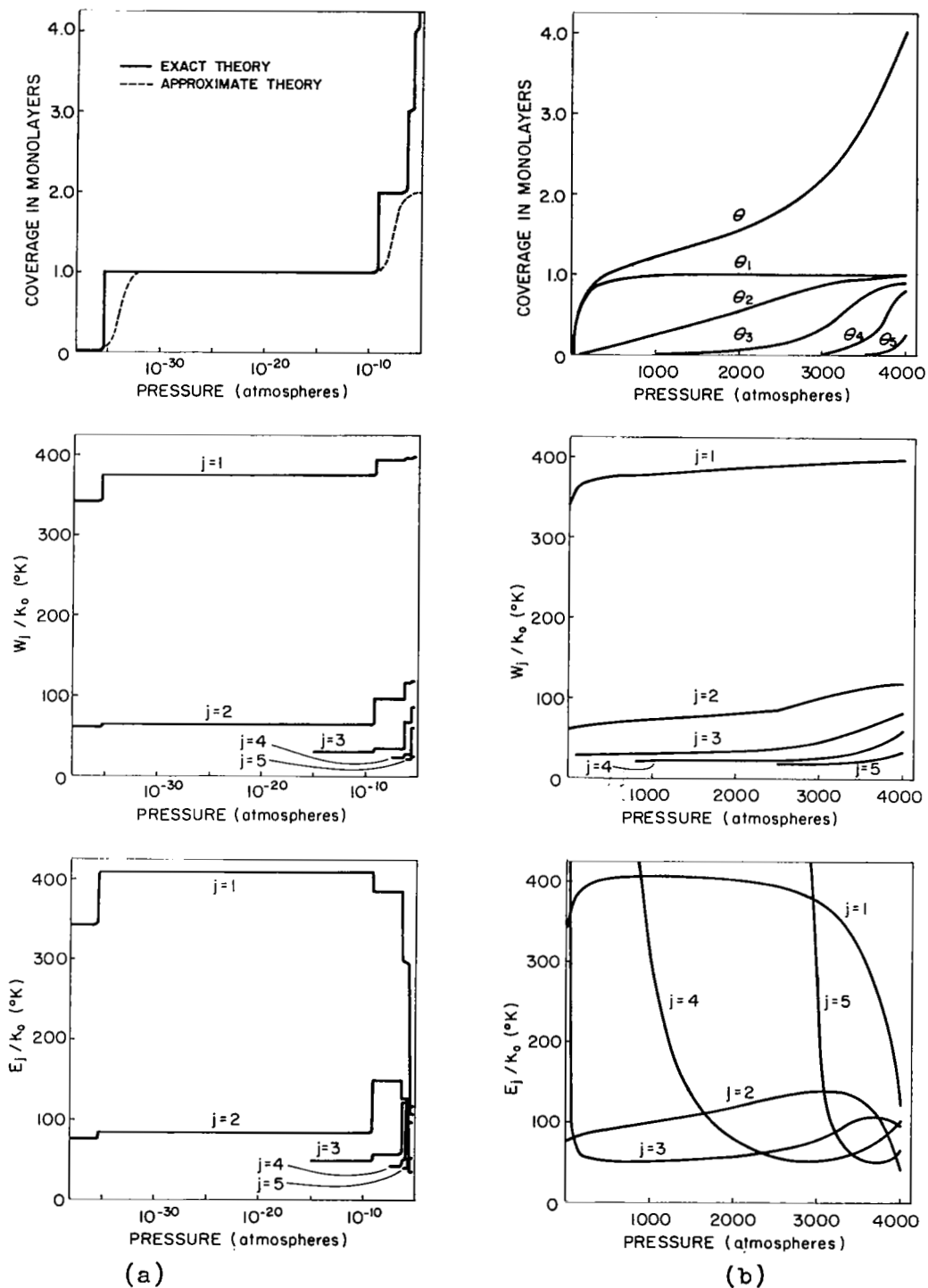
18

Fig. 4 - Adsorption Isotherms (Top) and Related Energies (Center and Bottom) for Helium on Glass at Two Temperatures: 4.28°K, Left Column (a), and 77°K, Right Column (b).

shown in Fig. 4b. The effective energies for layers one, two, and three show maxima, while the curves for layers three, four, and five show minima. The site availability in any layer being proportional to the cube of the coverage in the previous layer slows or prevents the migration of atoms from layer two to layer three at 100 atmospheres and from layer three to layer four at 2,300 atmospheres. However, the general appearance of partial layers above layer one is quite consistent with the crossings of effective energy lines in Fig. 4b. However, since the critical temperature for helium is exceeded, one does not expect condensation to a liquid to occur.

The theory also predicts a strong temperature dependence of the pressure at which first monolayer coverage becomes important. If the appearance of approximately 6 per cent of first monolayer is taken as a criterion for indicating a critical pressure, the following table of critical pressure versus temperature is obtained for helium on glass. The adsorption step features transform into smooth curves for temperatures above approximately 12°K because the $T^{2.5}$ factor essentially counterweights the collective energy effects above this temperature. However, Table III shows that the effectiveness of a cryopanel will be a strong function of the operating temperature when first monolayer is forming. A similar temperature dependence of second monolayer formation is expected, although the pressures will be higher (about 10^{-6} torr for second monolayer at 4.28°K for helium on glass).

TABLE III

PRESSURE AT WHICH SIGNIFICANT COVERAGE OF FIRST
MONOLAYER OF HELIUM ON POROUS GLASS OCCURS
AT VARIOUS TEMPERATURES

Pressure (torr)	Temperature (°K)
6×10^{-33}	4.28
1×10^{-27}	5.00
6×10^{-19}	7.00
4×10^{-12}	10.0
1×10^{-6}	15.0
6×10^{-4}	20.0
5×10^{-1}	30.0
$2 \times 10^{+1}$	40.0
$1 \times 10^{+3}$	60.0

The importance of effective W_s measurements for systems of cryopumping interest is illustrated by the fact that if W_s/k_o is lowered by 23.0°K, then the pressure for monolayer formation at 10°K is raised by one order of magnitude.

B. Experimental Investigation of Helium Cryopumping

The extreme high vacuum system developed under the present contract was used to evaluate cryopumping of helium gas on a stainless steel surface. Design of the system and experimental results are discussed in the two subsections below.

1. System design (experimental equipment): The extreme high vacuum system (see Fig. 5) was designed for general utility. The design and operational techniques employed provide the following features: effective pumping of all gases including inert species; significant reduction of the gases arising from desorption and permeation; and extremely sensitive partial pressure measuring techniques.

The small gas loads expected indicated that a sealed off system with getter-ion pumping and cryopumping would be the preferred type. Getter-ion pumping is most effective above 10^{-9} torr. Cryopumping is very effective at liquid helium temperature; however, the permissible gas load at a specified pressure is not well known. The applicable range of cryopumping will be clarified by this adsorption isotherm work.

The entire system is bakeable to 425°C and is connected via a bakeable valve to an external getter-ion pump used only during bakeout. By degassing the small getter-ion pump, while the external pump maintains a low pressure, the gettering surfaces of the internal pump are thoroughly cleaned so that the exchange process between trapped and newly pumped molecules is greatly reduced.

The desorption rate from the walls of the system is lowered by standard bakeout techniques (425°C is employed). Desorption is further reduced by cooling the entire system to liquid nitrogen temperature. The dewar shown in Fig. 5 serves as a liquid nitrogen container as well as a furnace jacket during bake-out.

The system is provided with ports for several pressure measuring devices. A short path ionization gauge (Varian Millitorr gauge, useful from 10^{-5} to 1 torr), a closed grid ionization gauge, a partial pressure analyzer, and a field emission microscope have been employed on the system simultaneously.
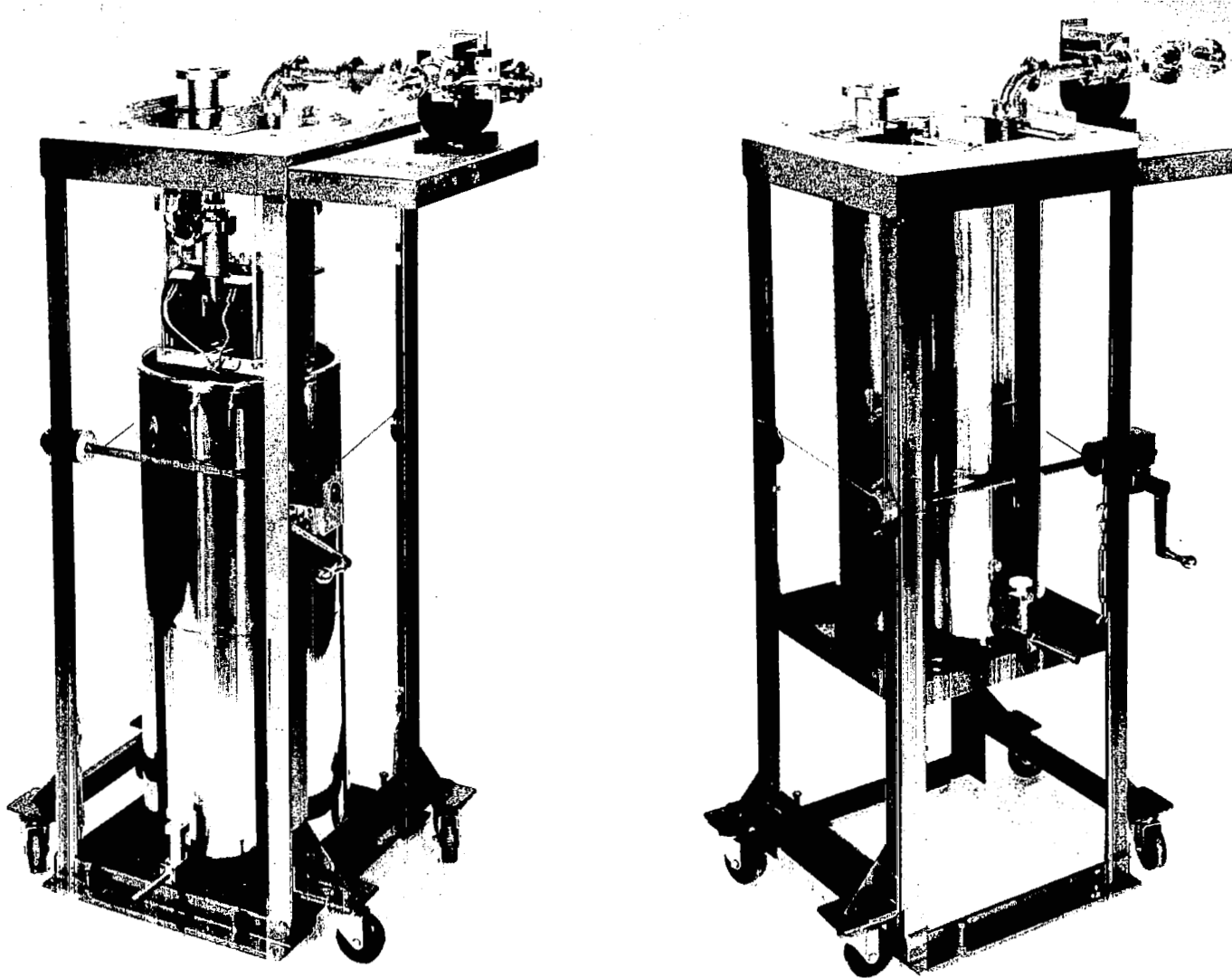
Fig. 5 - Extreme High Vacuum System for Experiments with: Liquid Helium Cryopanels, Field Emission
Microscopy, Partial Pressure Analysis, and UHV Gauges. The Entire Unit is Portable
and the Combination Furnace-Cryogenic Dewar is Movable for Easy Internal Access.

The partial pressure analyzer (see Fig. 6), which is an all metal and ceramic unit, was built to order by the General Electric Company. The unique feature of this tube is the design of the ionization chamber envelope. This design permits the analyzer to be mounted in line between a test chamber and a vacuum system. For example, the analyzer was directly attached between the cryopumped system, Fig. 5, and a field emission microscope. Further, because of the large conductances maintained throughout the manifold as a whole and particularly in the ionization chamber envelope, this tube may be considered to have a nude source. This tube is operated with a standard model 514 power supply unit and a 6.5 kilogauss electromagnet.

A Vycor glass diffuser is attached near the cryopanel to provide a pure helium source for the cryopumping experiments. The system used for adsorption experiments is shown in Fig. 7. Liquid nitrogen was introduced up to the level of the valve seat so that the entire sealed-off unit, with the exception of the Vycor diffuser, is maintained at liquid nitrogen temperature.

2. <u>Experimental results</u>: Adsorption data were obtained for helium on a stainless steel cryopanel which is consistent with: first monolayer coverage for pressures from $\sim 10^{-9}$ to 10^{-7} torr on the 4.28°K isotherm; second monolayer formation at 1.6×10^{-7} torr (indicated) for 4.28°K; second monolayer coverage from 2×10^{-7} to 10^{-4} torr; and third monolayer formation in the 10^{-4} torr range. Some correction factors are necessary to convert from gauge readings to actual pressure. Helium pressure values measured at the gauge position are one and five-tenths times the gauge values, assuming 77°K gas temperature. The thermal transpiration correction can be no less than 0.24 and may be 1.0 due to the large conductance between the cryopanel and gauge. Thus, second monolayer formation occurs for an actual helium pressure between 0.6 and 2.4×10^{-7} torr.

The amount of foreign atom adsorption on the cryopanel during the helium measurements was determined to be less than one part in 10^3 for the longest experiment. The ion gauge pumping speed for helium was also determined (0.015 liters/sec) since it is a competing process with cryosorption for helium gas removal. The area of cryopanel surface in contact with liquid helium was determined by means of a helium level sensor. The volume of the system for helium gas was measured to be 2.9 liters. All of the corrections and parameters listed above were combined to reduce the pressure data to coverage values on the cryopanel.
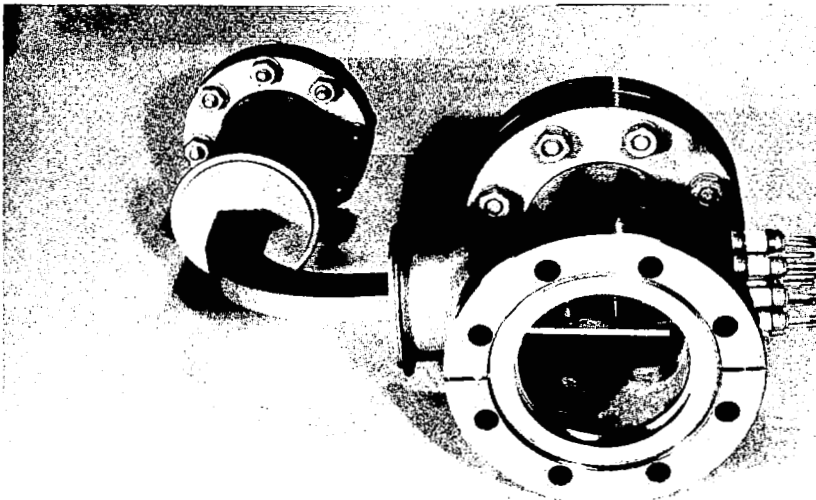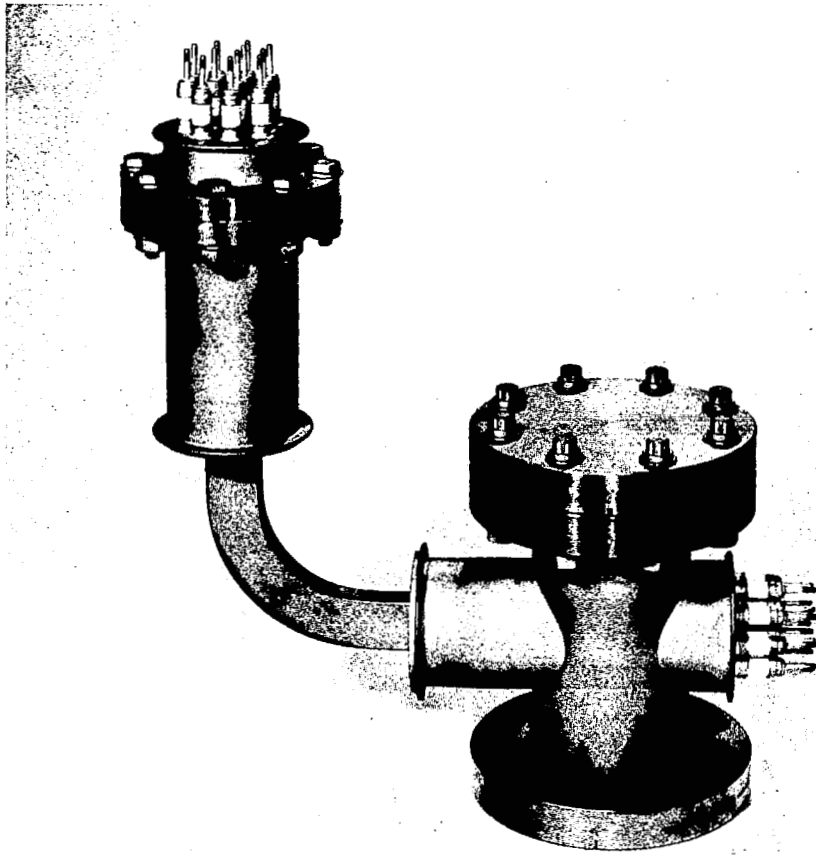
Fig. 6 - Partial Pressure Analyzer with Specially Constructed Ionization
Source Envelope. This Design Permits the Analyzer to be Used
with an In-Line Nude Ion Source Between a Test Chamber and a
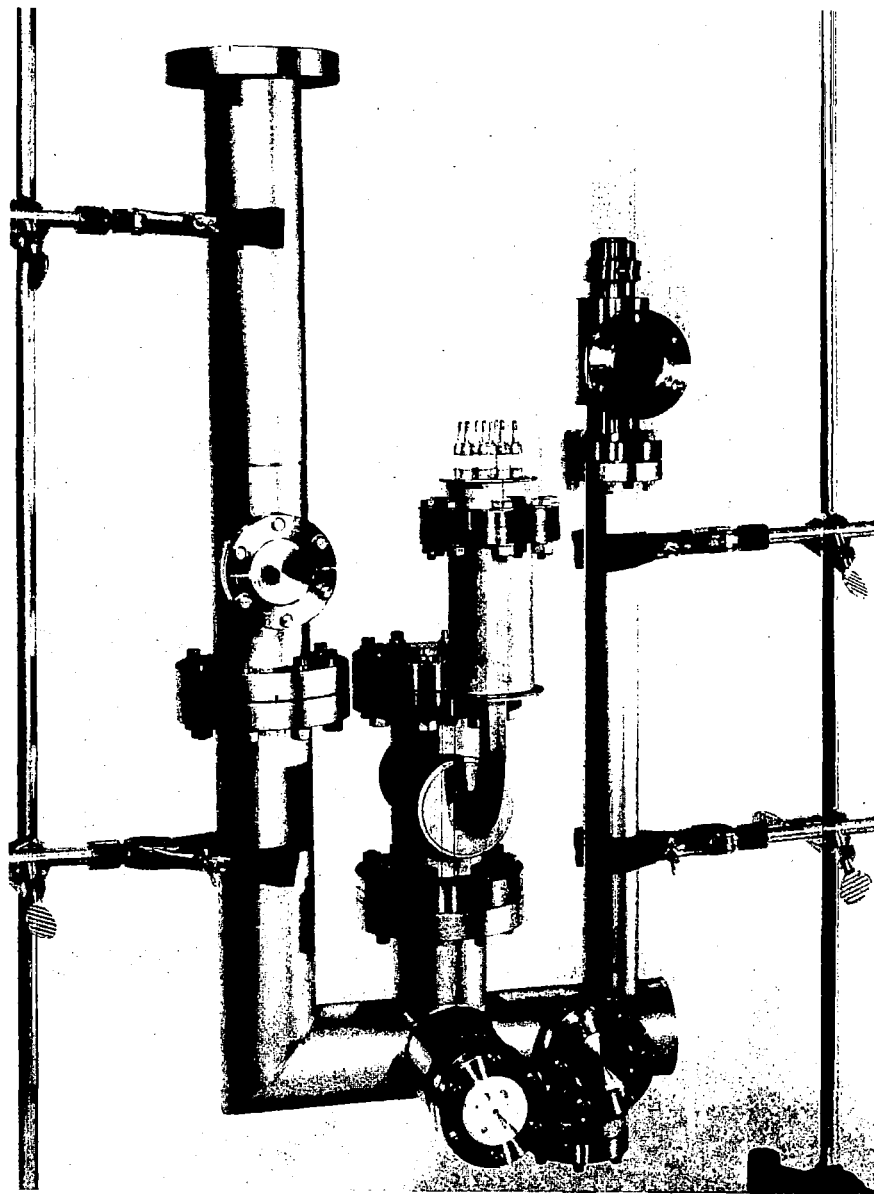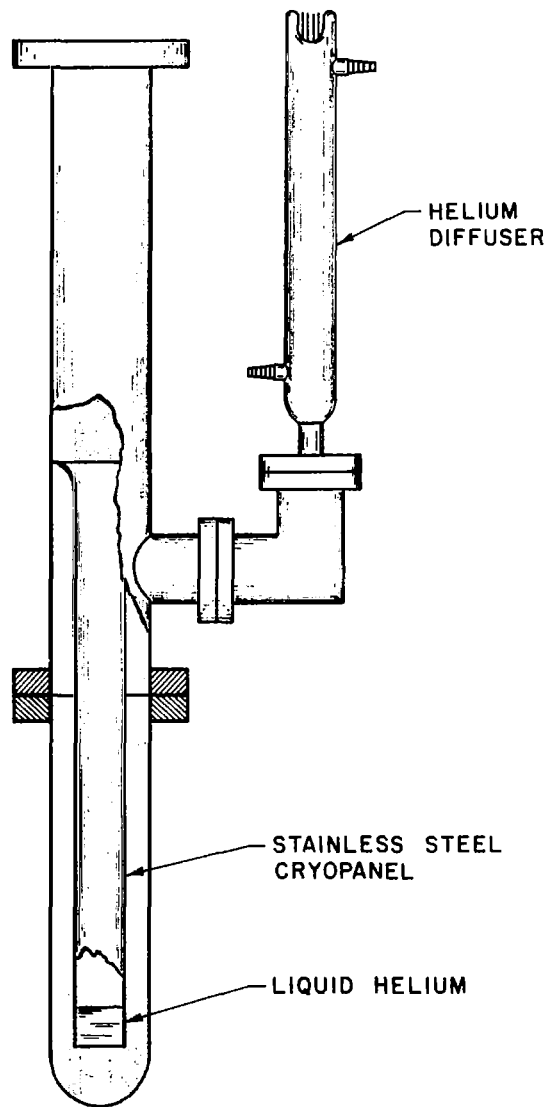Vacuum System.

Fig. 7 – System Used on Adsorption Isotherm Experiment. The Cryopanel (Liquid Helium
Filled Finger) and Diffuser Shown in the Drawing Form the Left Column
of the Vacuum System Shown in the Photograph.

V. A STUDY OF THE COLD WELDING ABILITY OF STRUCTURAL MATERIALS UNDER TYPICAL CONDITIONS OF USE

A guideline study of cold welding has been conducted. Three different cases pertinent to an over-all view of the possibilities for cold welding were considered. The first part was a review of previous work which strongly demonstrated the phenomenon of cold welding in an ideal case. The second part consisted of a set of tests which showed that light loads would not promote sufficient areas of contact between structural materials to give any measureable weldment even when the samples were outgassed in UHV. The third set of tests produced welding between structural materials under vibrational contacts with moderate loads. Some weldment occurred in air, but was, of course, more pronounced in vacuum.

A. Cold Welding Under Ideal Conditions

The first case (which was previously performed under another program) established the existence of the cold welding phenomenon both experimentally[6] and theoretically.[7] The study consisted of producing atomically smooth surfaces of lamellar solids such as mica in an extreme high vacuum so that they remained clean until they were allowed to reheal under their own attractive force. The energy required to separate the surfaces after reheal was just 13 per cent lower than the original energy expended to produce the surfaces from the bulk material.

These idealized experiments demonstrated that the cold welding phenomenon can occur at the highest level imaginable, i.e., to nearly the full cohesive energy of the bulk material. Two important conditions should be noted: (1) the lack of a compressive load to reheal the surfaces; and (2) the lack of added thermal energy (from frictional heating or otherwise); thus, true touch and contact cold welding was demonstrated. On the other hand, two other important conditions should also be noted: (1) the existence of atomically smooth surfaces for the rehealing tests so that the real area of atomic range contact was virtually 100 per cent of the projected surface areas tested; and (2) the existence of molecularly clean surfaces for the tests. Thus, the near bulk cohesive energy established is understandable under such ideal conditions since the surfaces could re-establish the atomic range spacing characteristic of the bulk material.

B. Lack of Cold Welding with Touch Contact of Structural Materials

An extended series of tests were completed regarding the adhesion of three structural materials exposed to vacuum and thermal outgassing. Previous work on this subject was reported in Ref. 1, pp. 61-68. The three materials examined were: aluminum alloy (x-2020-T6), titanium alloy (6Al, 4V) and stainless steel (type 301-1/2 HD). Since the same materials and techniques were employed in the previous study, the following report of these extended results will be in the form of a summary.

Figure 8 illustrates the technique employed to compare the adhesion by means of a measurement of the maximum angle of repose between the samples under light gravitational loading. Rotation of the vacuum chamber was possible at any time during the extended tests since small ion pumps or getter-ion pumps were used. All of the results fell within the 21 - 28° range shown.

Table IV lists some characteristic activation temperatures for the three materials studied. The relevant temperature for a thermally induced weldment is the Tammann temperature, since atomic diffusion (sintering) may occur around this temperature level (two-thirds of the absolute melting point value). However, if the melting point values of the bulk metals in question are compared with the Tammann temperatures of their surface oxide layers (see Table IV) some discrepancies are noted. For example, if two aluminum samples were in contact, their oxide layers could begin sintering at 1275°C; however, the bulk aluminum melts at just 660°C. Titanium and stainless steel do not show a similar contradiction; however, sintering of their oxide surfaces would require a temperature of 1000°C which is above the normal useful range. Therefore, no weldment due to sintering should occur for the three metals listed above.

The primary condition which must be established for weldment is an appreciable area of atomic range contact between the surfaces so that a significant reduction of the net free surface energy will occur. This condition was possible over the entire area of the atomically smooth mica layers. However, for the metal samples used in the second and third test series this condition is fulfilled by only a small fraction of the projected surface area. For touch contact or light loading below the yield strength of a material only the surface asperities, whose tips may be about 10^{-4} cm. in diameter, are in contact. Therefore, no significant degree of adhesion would be expected.

BAKE OUT   CONTACT   MAX. ANGLE
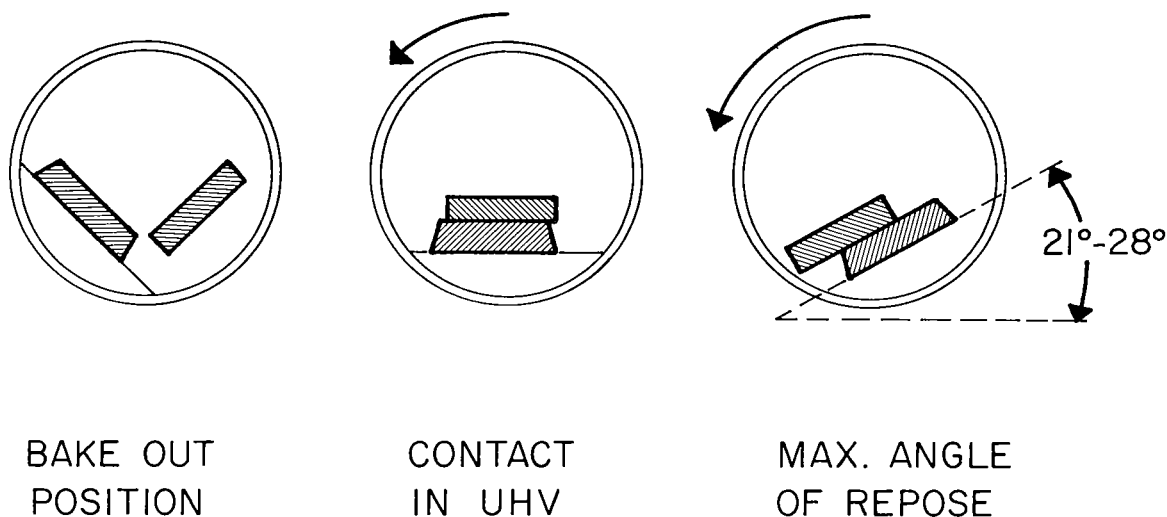POSITION   IN UHV   OF REPOSE

Fig. 8 - Illustration of a Technique for Alternately Exposing
the Surfaces of Two Samples to Vacuum Degassing
and Bringing the Same Surfaces Into Contact
for an Adhesion Measurement

        The data for polished surfaces (Table IV) verifies the expected lack
of adhesion since the maximum angle of repose measured in vacuum following de-
gassing was actually lower than the value measured in air for the same samples.
These results therefore indicate that the resistance to shear between the
sample pairs is dominated by static friction rather than a real adhesion bond.
Results obtained with polished surfaces could be influenced by a contaminant
film which would be eliminated by degassing whereas the results with original
surface textures would be dominated by metal asperity interlocking and there-
fore insensitive to outgassing. The data for all samples with original and
polished surfaces agree with this interpretation.

CHARACTERISTIC ACTIVATION TEMPERATURES

TEST MATERIAL	MELTING POINT TEMPERATURE (°C)	TAMMANN TEMPERATURE (°C)
ALUMINUM (X-2020-T6)	660	350
OXIDE Al_2O_3	2050	1275
TITANIUM (6% Al, 4% V)	1800	1100
OXIDE $Ti\,O_2$	1640	1000
STAINLESS STEEL (TYPE 301 $\frac{1}{2}$ HD)	∼ 1500	∼ 900
OXIDE (Cr_2O_3, $Ni\,O$, Fe_2O_3)	∼1700	∼1000

TABLE IV - Thermal properties relevant to the possibility of sintering between sample pairs of the three materials tested are tabulated above. The Tammann temperature represents the approximate threshold for thermally activated atomic diffusion. Thus, sintering would not be expected for the three materials tested since the oxide coatings would not be removed by vacuum exposure or touch contact abrasion and normal operation would not reach 1000°C.

COLD WELDING TESTS WITH STRUCTURAL MATERIALS UNDER VARIOUS CONDITIONS

TEST MATERIALS	TEST ENVIRONMENT TEMP. (°C)	ALTITUDE (MILES)	TIME (HRS.)	MAX. ANGLE OF REPOSE
ORIGINAL SURFACES	23	— AIR —		28°
Al (X-2020-T6)	23	350	500	28°
Ti (6% Al, 4% V)				
SS (TYPE 301 $\frac{1}{2}$HD)	350	165	100	28°
POLISHED SURFACES	23	— AIR —		23°
Al (X-2020-T6)	23	350	3150	21°
Ti (6% Al, 4% V)				
SS (TYPE 301 $\frac{1}{2}$HD)	350	165	200	21°

TABLE V - The results of cold welding tests under low nondeforming loads are tabulated above. The maximum angle of repose between sample pairs (see Fig. 8) gives a measurement of the static friction for separation in a shear mode. No differences occurred for samples with original surface texture; however, a 10 per cent decrease occurred in vacuum for polished samples which indicates decreased friction between clean surfaces compared to air contaminated surfaces.

The tabulated results, Table V, confirms the expectation that cold welding will not occur between lightly loaded metal samples with either the original surface texture of the sheet metal or with polished surfaces. (The polished surfaces also contact over a small area compared to the projected surface area.) Table V lists results for test conducted in air, after exposure to vacuum for periods up to 3,150 hr. and for thermal degassing plus vacuum exposure. Thus, test conditions simulated direct launch to the vacuum of a 350-mile earth altitude (i.e., vacuum of 3×10^{-10} torr attained without sample bake) and combined high temperature and UHV exposure.

C. Cold Welding Produced with Vibrational Contacts

The third set of experiments within the guideline study was designed to simulate actual conditions for structural components in contact with normal loading and under the influence of vibration (see Fig. 9). The following conditions were selected to simulate possible parameters during the first few minutes of launch when vibrational loads could be significant: (1) a normal load of 250 psi over the projected interface area; (2) a vibratory frequency of 5 cps; (3) a vibration amplitude of 0.03 in.; and (4) ambient temperatures with good thermal contact to each metal sample. (Interfacial temperatures during vibration were not recorded.) Pressures at the start of a launch period would be full atmospheric and would reduce rapidly with time; however, labyrinth type parts would outgas slowly, so that the vibratory tests conducted in air and moderate vacuum should be relevant.

Three sample materials were studied: aluminum (6061-T6), titanium (6Al, 4V), and stainless steel (301-1/2 HD). All three were tested in air and the stainless samples were tested in a moderate vacuum. A vacuum of 3×10^{-7} torr was attained without a bakeout, so that conditioning of the metal samples would be similar to the actual process of exposure to vacuum at high altitude.

Results are listed in Table VI as coefficient of friction values for the various samples and conditions described above. Two values are required for a coefficient of friction determination: the normal load and the frictional force. Normal loads were set at 3.9 lb., since the projected area of contact was 1/8 in. x 1/8 in. and a 250 psi value was desired. Both normal loads and frictional forces were measured with a spring balance. A set of data was determined before vibration and at the periodic intervals listed in Table VI. The first measurement following a period of vibration is labeled (a), a second measurement is labeled (b). For each case in which the (b) value was lower than the (a) value, we may conclude that a vibrationally induced weld was broken by the first act of measurement (a). A second measurement then requires a lower "frictional force" to initiate a shearing motion between the sample faces.
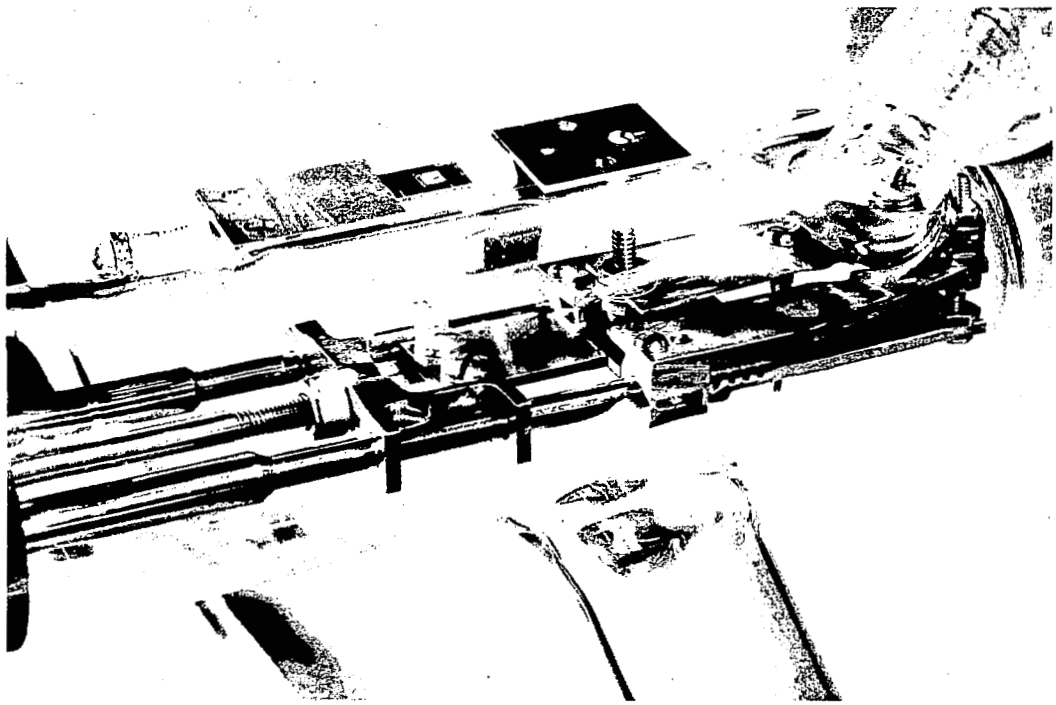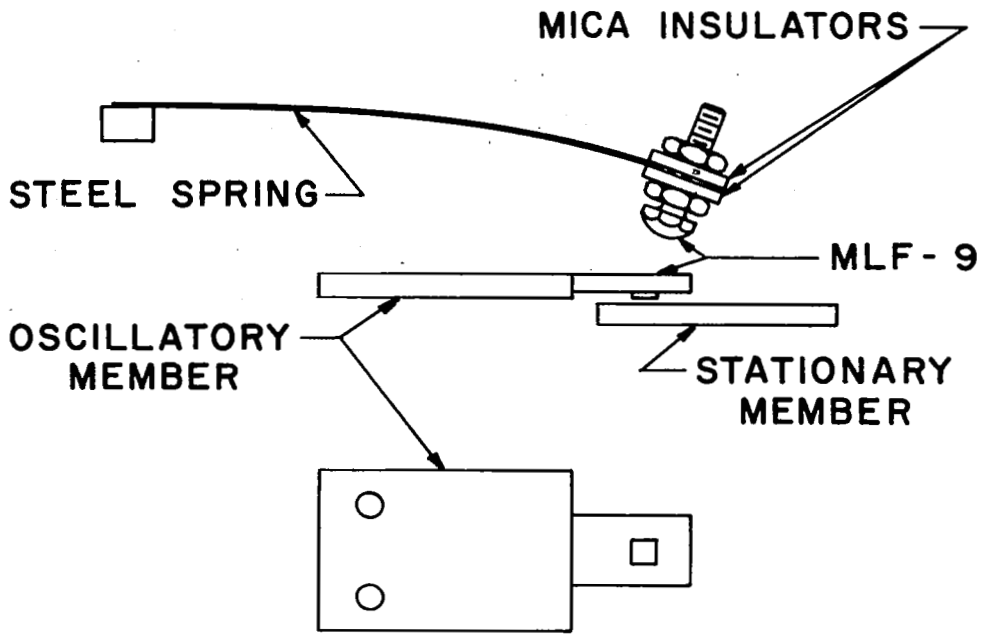
Fig. 9 - Apparatus for Vibratory Cold Welding Tests. The Spring Loading
Device and a Sample Pair Are Shown in the Drawing. The
Assembled System and Another Sample Pair Are Seen
In the Photograph.

| | | | | STATIC FRICTION | |
TEST MATERIAL	ATMOSPHERE (TORR)	TIME (MIN)	NO. OF CYCLES	FORCE (LBS)	COEFFICIENT
Al ON Al (6061-T6)	760	0	0	1.6	0.41
		5.0	1,500	(a)3.6	0.92
				(b)3.2	0.82
Ti ON Ti (6 Al, 4 V)	760	0	0	2.2	0.56
		2.5	750	2.2	0.56
		4.5	1,350	(a)3.5	1.0
				(b)2.1	0.54
S.S. ON S.S. (301 1/2 HD)	760	0	0	0.8	0.20
		2.5	750	(a)3.0	0.77
				(b)1.0	0.26
		5.0	1,500	2.7	0.69
S.S. ON S.S. (301 1/2 HD)	3×10^{-7}	0	0	0.75	0.20
		0.5	150	(a)5.0	1.3
				(b)1.75	0.45
		1.0	300	(a)5.5	1.4
				(b)2.5	0.64
		2.5	750	(a)6.5	1.7
				(b)2.5	0.64

TABLE VI - Results reported in terms of the static coefficient of friction for cold welding tests performed with vibrational contact for various conditions. The first measurement following a period of vibration is listed as (a) and a second measurement as (b). The component of weldment is broken during the first shear measurement (a) so that the difference between (a) and (b) indicates the amount of cold welding.

Another interesting change of frictional values may be noted between the zero reading taken before vibration tests and the (b) values. After the component of weldment is broken, the coefficient of friction would be expected to return to the initial value. However, the plowing component of friction is different after the surfaces have been deformed by a testing cycle. Considerable plowing and metal transfer has occurred so that the coefficient of friction is higher by as much as two times for aluminum in air and three times for stainless steel in vacuum. However, even larger increases in total shear strength, as measured following a vibrational test, are recorded: e.g., by a factor of 2 for titanium in air, by 3.5 for stainless steel in air, and by 7.5 for stainless steel in vacuum. The increment of shear strength above the frictional value is interpreted as a component of weldment. Thus, vibrational motions under moderate loading cause a breakdown of the oxide layers and deformation of the interface surfaces, so that a larger area of real contact exists.

The amount of weldment observed in these short term tests in air and moderate vacuum environments is sufficient to demonstrate the significance of the cold welding problem for moving or vibrating contacts.

VI. A PRESSURE CALIBRATION STUDY FOR THE ULTRA-HIGH VACUUM RANGE INCLUDING THE USE OF A FIELD EMISSION MICROSCOPE

A series of tests was conducted with cold cathode magnetron gauges in their original condition. Another series of experiments was carried out with the gauges following cesiation treatments. A fundamental study of gas dynamics by means of an electron field emission microscope in conjunction with a sensitive partial pressure analyzer is also reported. A large quantity of data has been recorded and several new characteristics have been determined. The response of Redhead and Kreisman gauges over their entire range of operation is plotted. The design and initial results of a field emission microscope operated on an ultra-high vacuum system are also described.

A. Techniques Employed

Comparative pressure measurements with hot filament ionization gauges and cold cathode magnetron gauges were made by a conductance regulated flow

method using helium gas and a continuously pumped open type UHV system (see Fig. 10). The flow of helium was accurately regulated since there was essentially only one source and one sink for helium in the system. The source was a Vycor helium diffuser which purifies the gas as well as regulating the flow rate. The purity level is very high which assures the bulk of gas with the desired features: low boiling point and chemically inert. Therefore, the flow rate will not be appreciably altered by physical or chemical adsorption within the system, i.e., by cryopumping in the liquid nitrogen cold traps or by gettering on glass walls or metal parts of the system. Thus, the pressure ratio remains constant for values within the molecular flow range, which are of interest in this study of gauges.

Ionization gauges were used to establish the value of conductance between the reference and test gauge positions. A magnetron gauge was then placed in the test position and a range of pressure values was covered by varying the flow rate of helium gas. In summary, the system used was carefully planned for controlled gas flow tests by providing a constant evacuation speed through a series of mercury diffusion pumps and a regulated source of pure helium gas through a glass diffuser.

The characteristics of both Redhead and Kreisman type magnetron gauges were determined over their entire operating ranges. The pressure ratio method described above was used for the study of both magnetron gauge types. In addition, the Kreisman gauges were studied by direct comparison to ionization gauges, since the commercial ion gauge employed (Varian type UHV-12) covers the full operating range of the commercial Kreisman gauge. A cesiation treatment was developed and employed to gain a better understanding of the operation of magnetron gauges (see Fig. 11).

Pressure values were determined by both the pressure ratio and direct reading methods described above, using ionization gauges with constant, monitored, emission current. The ion current values, plotted as pressure, were corrected by subtracting the total residual currents (including x-ray generated photo current and surface-generated ion current). Ion current values were measured with a Cary model 35 vibrating reed electrometer. High voltage settings were regularly monitored with a sensitive Electrostatic Voltmeter.

B. Cold Cathode Magnetron Gauge Characteristics

Results from a large number of tests with commercially available cold cathode magnetron gauges of two types: NRC-Redhead gauges, and GCA-Kreisman gauges are reported in subsections (1) and (2) below.

MAGNETRON AND ION GAUGE COMPARISONS
BY A
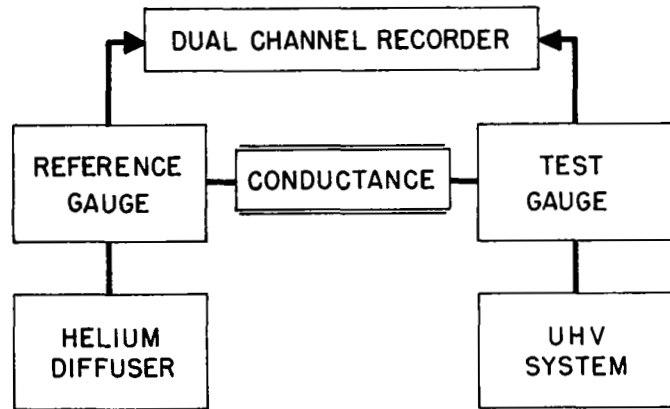# CONDUCTANCE REGULATED FLOW METHOD

Fig. 10 - The Pressure Ratio System for Gauge Comparison is
        Shown in Block Diagram Above. Ion Current Re-
        sponse From the Reference and Test Gauges Are
        Simultaneously Recorded. A Continuously Variable
        Vycor Glass Diffuser Provides a Pure Helium
        Supply. A Glass System with Mercury Diffusion
        Pumps is Used to Maintain a Uniform Flow of
        Helium Gas for Pressures Throughout the UHV
        Range.
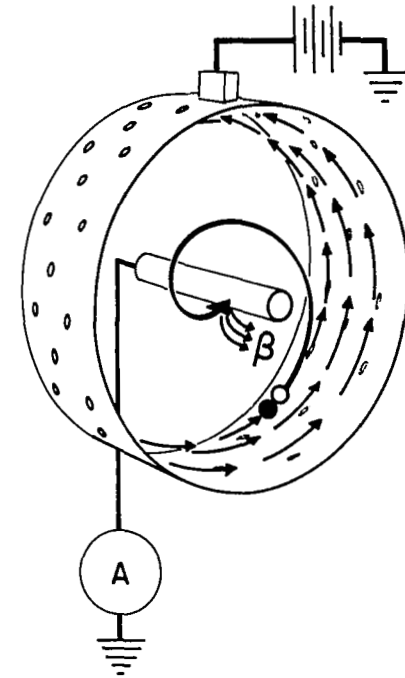
Fig. 11 - Basic Configuration of Magnetron
        Pressure Gauge. Ions and Cathode
        Generated Electrons Are Measured
        by the Ammeter, A . The Ions Are
        Formed by Gas Impacts with the
        Electron Cloud Near the Anode.
        Cesiation Raises the Escape Proba-
        bility β for Avalanche Initiating
        Electrons.

1. Response of Redhead gauges: The series of experiments with Redhead gauges has shown essentially linear ion current to pressure response for the range above 3×10^{-9} amp. A sharp break occurs at 3×10^{-9} amp followed by a gradual deviation from linearity as pressure decreases. The response below the break point has been approximated by a straight line in Figs. 12 and 13 for illustration purposes. The actual response of a clean, noncesiated Redhead gauge is given in Fig. 14.

The current to pressure response of uncesiated gauges below the break point was found to vary for different tubes. A logarithmic slope of 1.65 was the most repeated value; however, one tube gave a value of 2.2, while another tube gave an essentially infinite value, since it went immediately to cutoff at the normal break point.

The series of experiments with cesiated Redhead gauge tubes has shown a consistent value of 3×10^{-9} amp for the electronic break point and repeated values of 1.35 to 1.38 for the logarithmic slope of the response curve below the break. These later values are more accurate than the value of 1.43 reported previously.[1] An "electronic break" is referred to here rather than a pressure level break, since the break point in pressure terms may be lowered by a cesiation treatment.

Figure 12 gives an indication of the improvement which cesiation affects upon the response of magnetron gauges. Noncesiated gauges deviate from linear response at a pressure of 7×10^{-10} torr and fall approximately one order of magnitude below linearity for a pressure of 2×10^{-11} torr, as shown in Fig. 12. A cesiated gauge, with a moderate sensitivity rise of two times, goes into the nonlinear region at one half of the previous value or 3.5×10^{-10} torr and follows a response line of different slope so that it is in error by only 2.5 times (rather than 10 times) for the same pressure value of 2×10^{-11} torr.

The characteristics which have been observed for Redhead magnetron gauges may be outlined as follows: (1) the break from linear response occurs consistently at the same value of ion current for various gauge tubes; (2) the nonlinear response is different for various gauge tubes; and (3) a lower limit for operation of the magnetron (i.e., a threshold or cutoff level) exists (see Fig. 13).

The characteristics which result from a cesiation treatment may be outlined as follows: (1) the ion current to pressure response is raised (i.e., a sensitivity rise); (2) the nonlinear response of various tubes is raised and stabilized at one value (S = 1.35); and (3) ion current threshold or cutoff corresponds to a lower pressure value (approximately 1×10^{-12} torr).
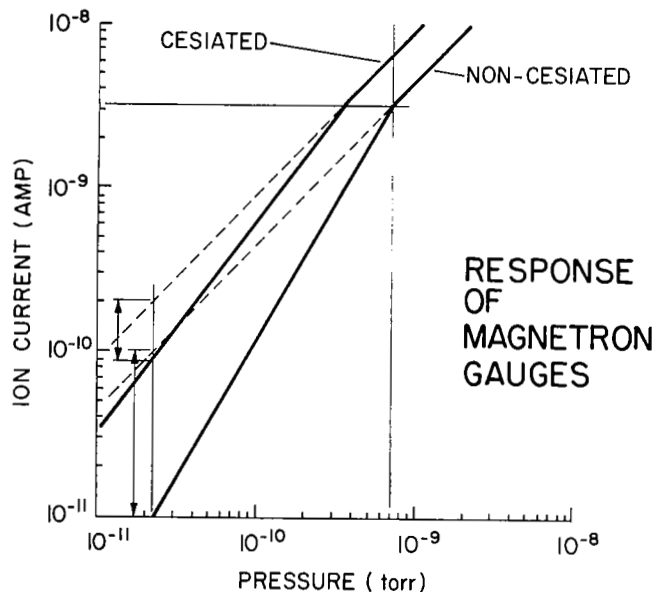
Fig. 12 – The Response of Redhead Magnetron Gauges
May be Increased by a Cesium Treatment.
The Sensitivity Rise in the Linear Por-
tion of the Characteristic Curve is by a
Factor of Two. A Larger Variation in
Nonlinear Behavior is Indicated. For a
True Pressure of 2.2×10^{-11} Torr, the
Average Noncesiated Gauge Reads 2.2×10^{-12} Torr While a Cesiated Gauge Reads
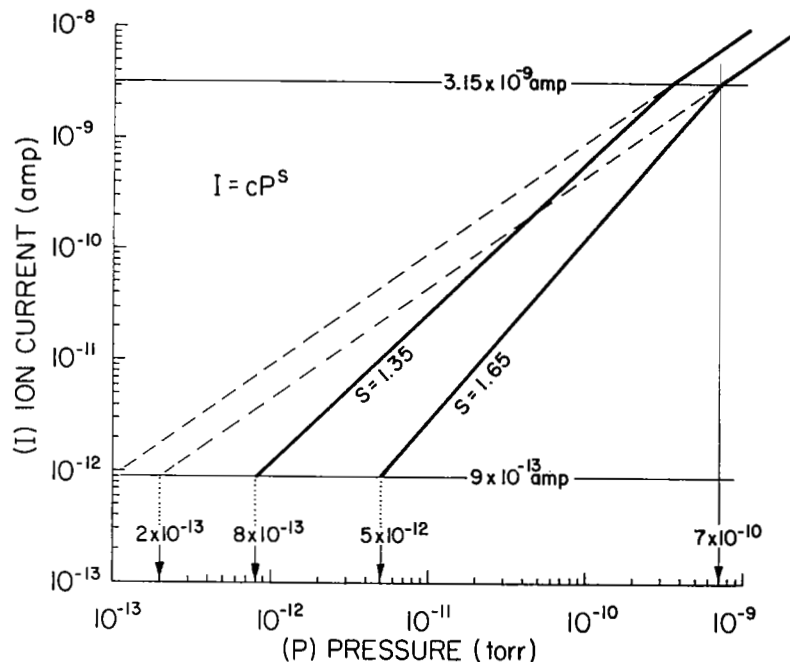1.0×10^{-11} Torr. Thus, an Error of 10
Times is Reduced to 2.2 Times.

Fig. 13 – Nonlinear Response Occurs Below 3×10^{-9}
Amps and Varies for Individual Redhead
Gauges. The Slope of the Response Curve
is 1.65 For a Representative Gauge (Best
Response is Shown in Fig. 14). The Slope
for a Cesiated Gauge is 1.35 Giving the
Possibility of a Lower True Pressure Cor-
responding to the Cutoff Current of 9×10^{-13} Amp. Note That the Response Curves
Are Approximated by Straight Lines in This
Figure, Whereas the Actual Response of a
Redhead Gauge (Fig. 14) Shows an Ever
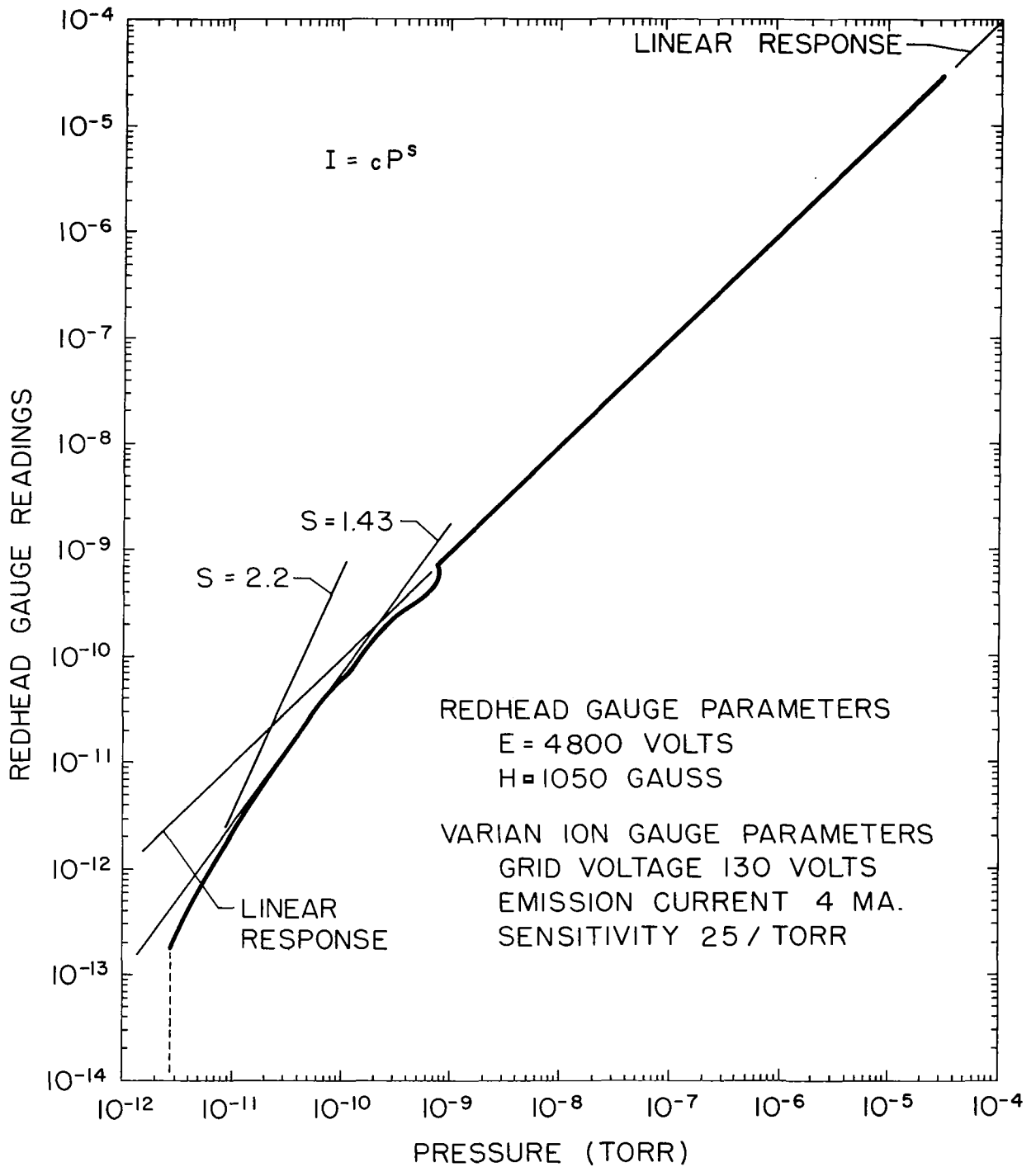Changing Slope in the Nonlinear Region.

Fig. 14 - Indicated Pressure from a Redhead Gauge Versus True Pressure
(as Determined by the Pressure Ratio Method) is Plotted
Above. The Approximate Nonlinear Response of 1.43
Represents the Best Gauge Whereas an Average
Gauge Response Approximates a 1.65 Slope.

2. <u>Response of Kreisman gauges</u>: The response of commercial Kreisman (Geophysics Corporation of America) gauges is plotted in Fig. 15. Since the full operating range of the Kreisman gauge is above 1 x 10^{-10} torr actual pressure, it was possible to run direct comparisons with closed grid ion gauges. The ion gauge measurements were corrected for total residual current values. The response curves obtained from the pressure ratio system, where the ion gauge is biased above its background limit, then agreed with the direct comparison response curves. Figure 15 is therefore a combination of response curves obtained by both methods.

C. Field Emission Microscope

A field emission microscope and the accompanying power supply was designed and constructed. A sketch of the tube is shown in Fig. 16. The pyrex envelope has an electrically conductive aluminum deposit on the inner wall which connects to the metal flange and acts as a grounded anode. The tip is then attached through an insulating glass press to the negative terminal of a power supply. The tip may be thoroughly cleaned by passing a current through the two supporting leads.

Electrons are drawn from the hemispherical end of the tip by direct field emission. The electric field (E) on a spherical conductor of radius (r) is given by $E = V/r$, where (V) is the applied potential. Considering the work function of tungsten, it is necessary to apply a field as high as 10^8 v/cm to draw electrons from the cold metal, i.e., without the aid of added thermal energy. The tungsten and platinum emitter tips, used in the microscope, have various radii from 300 to 800 Å. Field strength values (calculated from the equation above) for the various size tips are from 6 x 10^8 to 10^9 v/cm, so that a copious supply of electrons was available.

The inner side of the tube face is coated with a fluorescent screen to convert electrons to visible light. Visual observations and photographic recordings were made from above the flat glass face. An area of screen may be accurately correlated with an area of the tip so that data recorded from the screen may be normalized to unit area of the tip. The tube size and position on the extreme high vacuum system was planned so that the screen would protrude 1 in. above the liquid nitrogen level, thus permitting undistorted photography.

The rectilinear magnification obtained from the ratio of cathode-anode distance to tip radius will vary from about 2 to 4 million times with the 300 to 800 Å tips mentioned above. Thus, dimensions in angstrom units on the tip were magnified to tenths of a millimeter size on the screen.
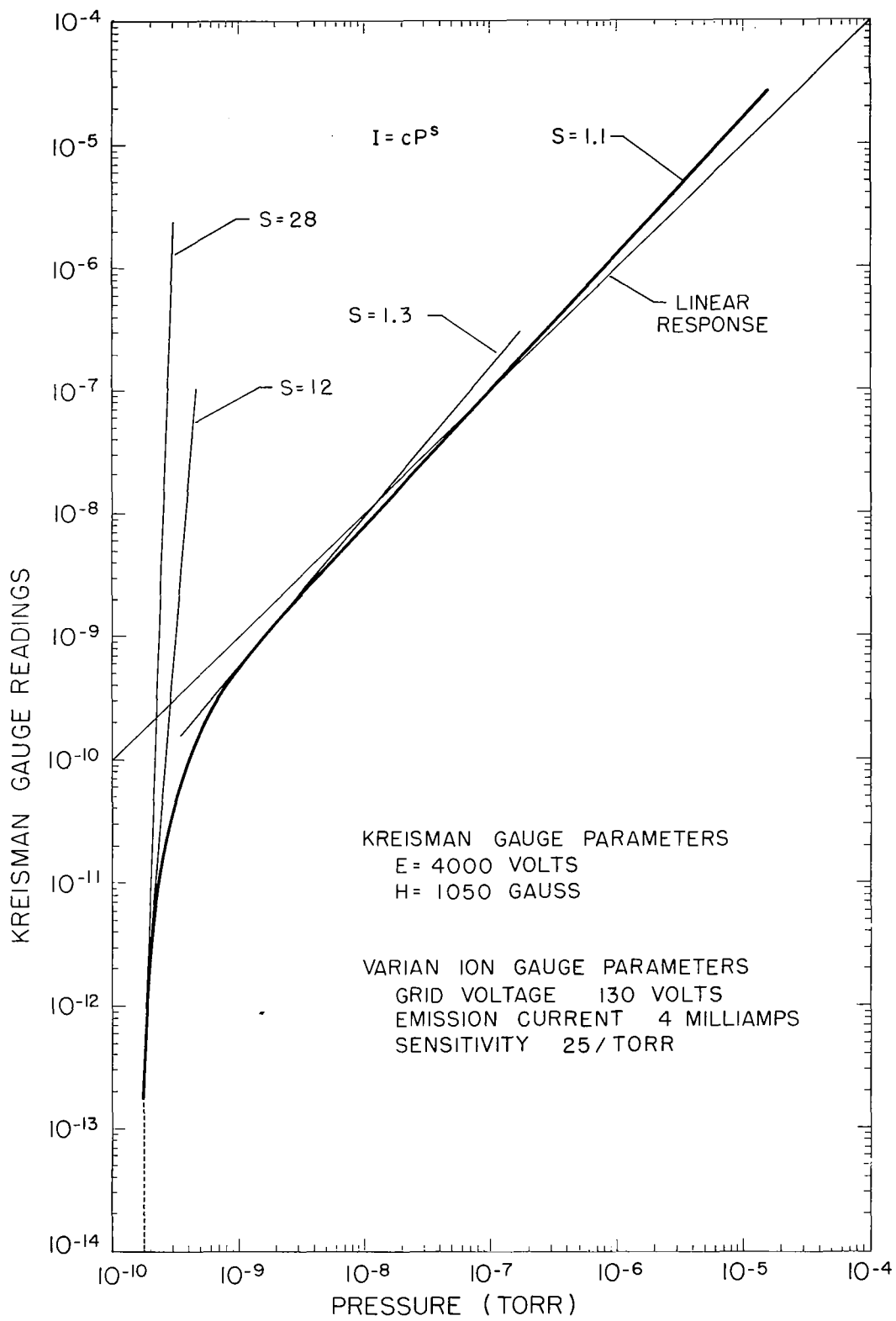
Fig. 15 - Indicated Pressure Versus True Pressure for Kreisman Gauges
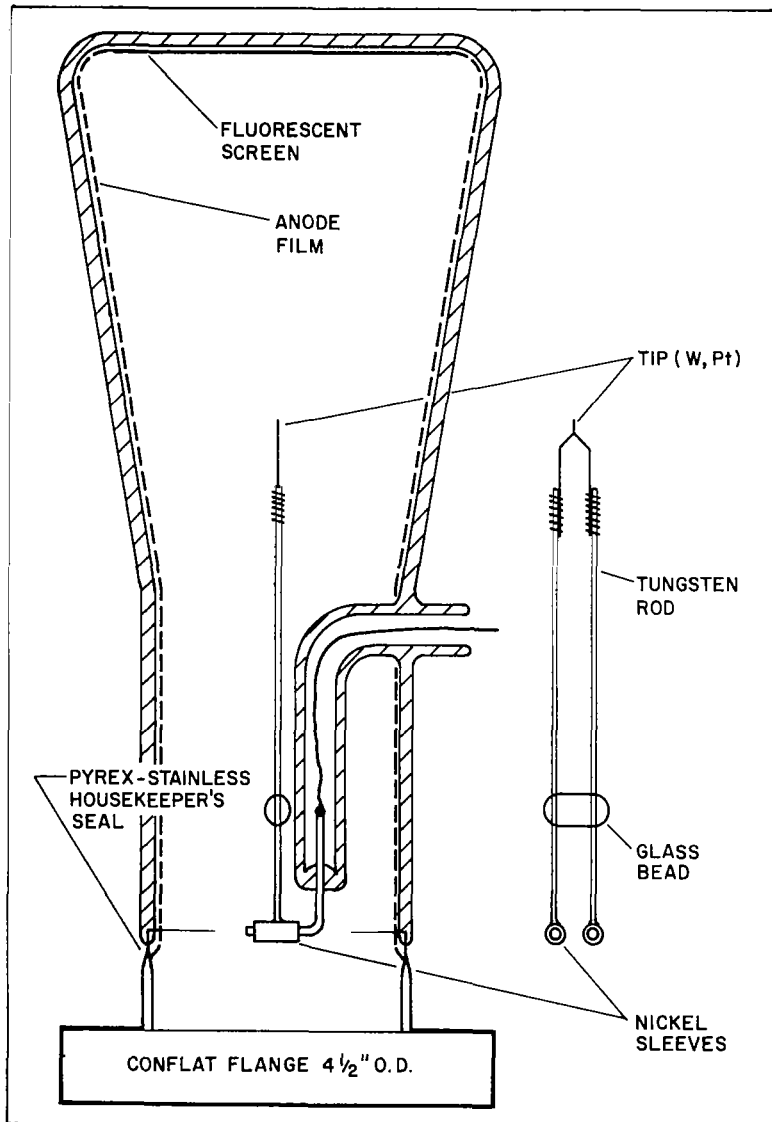
Fig. 16 - Field Emission Microscope Tube Details. Tip
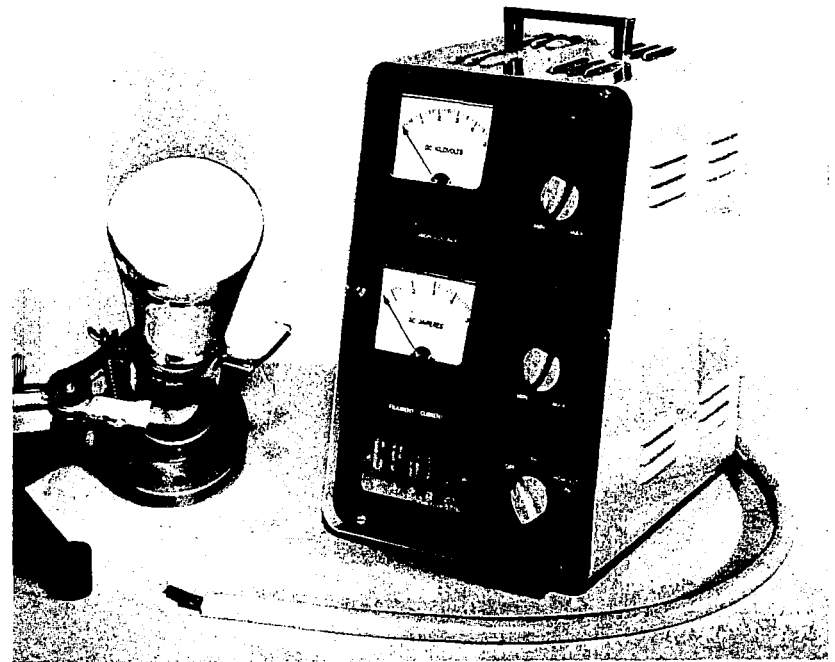Assembly and Support Rods Are Easily
Removed from Press Fit Mountings.

Fig. 17 - Field Emission Microscope Tube (Not Mounted)
and Power Supply Which Can Heat the Tip
While an Emission Pattern is Being Viewed

The electron field emission microscope was specially constructed by the Central Scientific Company according to the design given above. Figure 17 shows the electronic control unit and microscope tube.

The microscope tube is constructed of pyrex glass and stainless steel. A housekeeper's type glass to metal seal is incorporated for use in liquid nitrogen. This seal does not employ the usual kovar metal to graded glass connection. The pyrex glass is sealed directly to a stainless steel tube which has been reduced to a thin wall in the vicinity of the seal. Variations of thermal expansion between the glass and metal may be accommodated by the thin wall stainless tube over a wide temperature range. The microscope tube is exposed to temperatures from 450 to -195°C for bakeout and liquid nitrogen operation.

The control unit shown in Fig. 17 provides a high voltage supply for electron emission and a filament current supply for degassing the tip. The high voltage source is continuously variable from 0 to 5,000 v. with positive ground for safety. That is, the conductive coating on the glass microscope tube is attached to ground (through the metal flange) and serves as a grounded anode. The metal tip which is safely isolated from the metal flange may be driven as low as 5,000 v. below ground. Contaminants on the metal tip may be removed by electrically heating the tip holder. A variable filament current supply is provided for this purpose. This later power supply is well isolated from ground and it floats on the negative 5,000 v. output, thus giving the ability to heat the tip while operating the microscope. Direct observation of the degassing process has been particularly interesting and useful.

The field emission pattern obtained from a clean platinum tip is shown in the first view of Fig. 18. The hexagonal shape seen near the center of the fluorescent screen is an image of the terrace edge around the 111 crystal facet. Six other outlines are seen around the center image; they represent 210 facets as determined by a gnomonic projection. The three other patterns shown in Fig. 18 are from different operations of a platinum tip in the presence of electropositive sodium atoms. A buildup of the number of single bright spots was observed by means of a series of photographs taken with a time pulsed (motor driven) Praktina camera.

The spots were examined carefully according to a criterion which has been employed previously to distinguish single atom images from images produced by atomic agglomerates. This criteria consists of a carefully controlled desorption process along with a constant monitor of spot intensity. Since the spots did not show any intensity degradation, they would be assigned as single
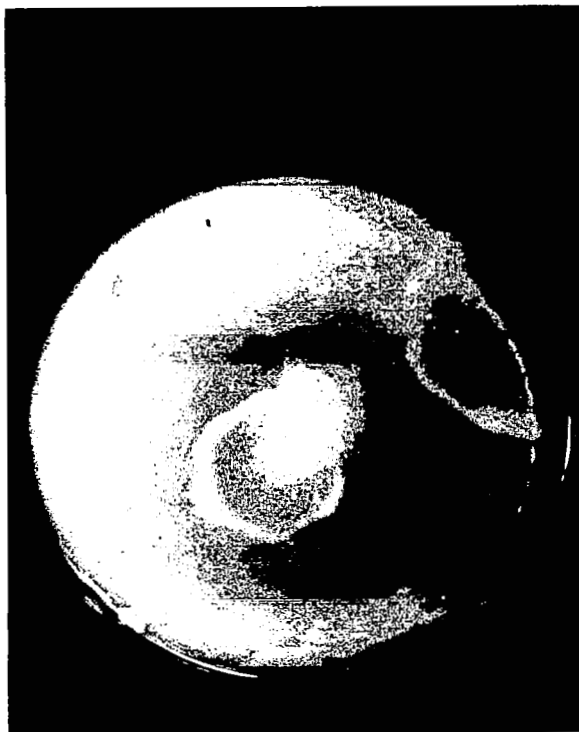
Fig. 18 - Field Emission Microscope Images Using a Platinum Tip. Crystal Facets
         Are Outlined by Electron Emission (upper left). The Three Additional
         Views Were Taken with Reduced Field so That Adsorbed Atoms Are Clearly
         Visible. This Technique is Being Employed to Study Basic Gas
         Dynamics as a Determination of Pressure.

atom images by this criterion. That is, unit desorption of the spots occurred which indicates a unit source for the image rather than an agglomerate. The observation and measurement of single atom gas dynamics, as indicated above, can be used for a pressure calibration study.

REFERENCES

1. Bryant, P. J., C. M. Gosselin, and L. H. Taylor, NASA CR-84 (1964).

2. Florescu, N. A., _Australian J. Appl. Sci._, _8_, 305 (1957).

3. Florescu, N. A., _Vacuum_, _10_, 250 (1960).

4. Alexander, P., _J. Sci. Instr._, _23_, 11 (1946).

5. Kennedy, P. B., _1961 Trans. of the Eighth Vacuum Symposium and Second International Congress_, 320, Pergamon Press (1962).

6. Bryant, P. J., "Cohesion of Clean Surfaces and the Effect of Adsorbed Gases," _1962 Trans. of the Ninth Vacuum Symposium_, Macmillian Press (1962).

7. Bryant, P. J., L. H. Taylor, and P. L. Gutshall, "Cleavage Studies of Lamellar Solids in Various Gas Environments," _1963 Trans. of the Tenth Vacuum Symposium_, McGregor Werner Press (1963).